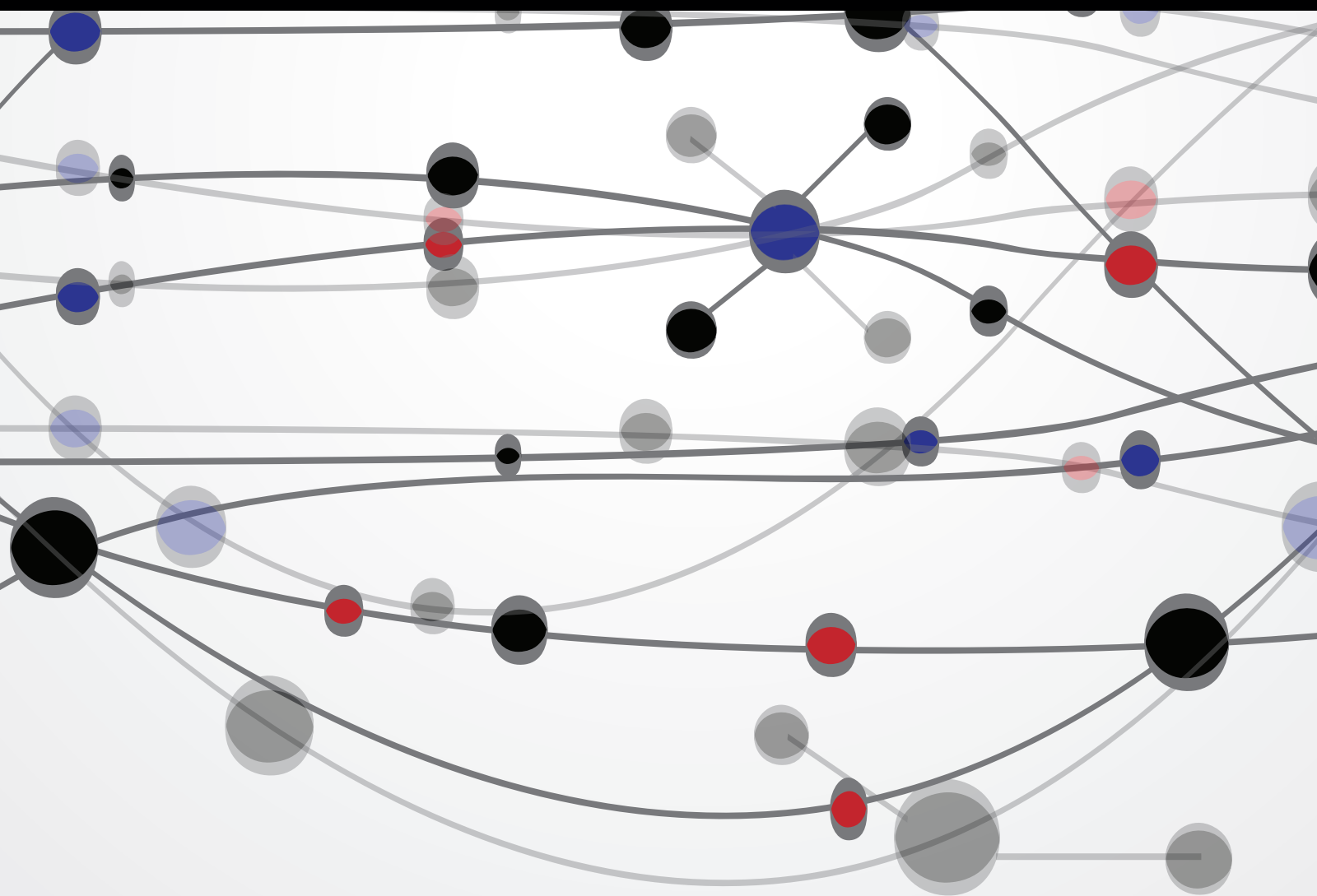


Narrow-Gap Semiconductors and Low-Dimensional Structures for Optoelectronic Applications

Guest Editors: Fangyu Yue, Satyabrata Jit, and Weida Hu





Narrow-Gap Semiconductors and Low-Dimensional Structures for Optoelectronic Applications

The Scientific World Journal

Narrow-Gap Semiconductors and Low-Dimensional Structures for Optoelectronic Applications

Guest Editors: Fangyu Yue, Satyabrata Jit, and Weida Hu



Copyright © 2014 Hindawi Publishing Corporation. All rights reserved.

This is a special issue published in "The Scientific World Journal." All articles are open access articles distributed under the Creative Commons Attribution License, which permits unrestricted use, distribution, and reproduction in any medium, provided the original work is properly cited.

Contents

Narrow-Gap Semiconductors and Low-Dimensional Structures for Optoelectronic Applications, Fangyu Yue, Satyabrata Jit, and Weida Hu
Volume 2014, Article ID 492521, 2 pages

Second-Order Nonlinearity in Triangular Lattice Perforated Gold Film due to Surface Plasmas Resonance, Renlong Zhou, Xiaoshuang Chen, Yingyi Xiao, Bingju Zhou, Lingxi Wu, Xiaojuan Liu, Yongyi Gao, and Jie Zhan
Volume 2014, Article ID 284929, 6 pages

Valence Band Structure of $\text{InAs}_{1-x}\text{Bi}_x$ and $\text{InSb}_{1-x}\text{Bi}_x$ Alloy Semiconductors Calculated Using Valence Band Anticrossing Model, D. P. Samajdar and S. Dhar
Volume 2014, Article ID 704830, 4 pages

Effect of Same-Temperature GaN Cap Layer on the InGaN/GaN Multiquantum Well of Green Light-Emitting Diode on Silicon Substrate, Changda Zheng, Li Wang, Chunlan Mo, Wenqing Fang, and Fengyi Jiang
Volume 2013, Article ID 538297, 4 pages

Donor-Like Surface Traps on Two-Dimensional Electron Gas and Current Collapse of AlGaIn/GaN HEMTs, Chen-hui Yu, Qing-zhou Luo, Xiang-dong Luo, and Pei-sheng Liu
Volume 2013, Article ID 931980, 6 pages

Phosphorescent Molecularly Doped Light-Emitting Diodes with Blended Polymer Host and Wide Emission Spectra, Jun Wang, Jun Gou, and Weizhi Li
Volume 2013, Article ID 954146, 5 pages

Optical Limiting Using the Two-Photon Absorption Electrical Modulation Effect in HgCdTe Photodiode, Haoyang Cui, Junjie Yang, Jundong Zeng, and Zhong Tang
Volume 2013, Article ID 245310, 4 pages

The Effect of Metal-Semiconductor Contact on the Transient Photovoltaic Characteristic of HgCdTe PV Detector, Haoyang Cui, Yongpeng Xu, Junjie Yang, Naiyun Tang, and Zhong Tang
Volume 2013, Article ID 213091, 5 pages

Editorial

Narrow-Gap Semiconductors and Low-Dimensional Structures for Optoelectronic Applications

Fangyu Yue,¹ Satyabrata Jit,² and Weida Hu³

¹ Key Laboratory of Polar Materials and Devices of MOE, East China Normal University, Shanghai 200241, China

² Department of Electronics Engineering, Indian Institute of Technology (BHU), Varanasi 221005, India

³ National Laboratory for Infrared Physics, Shanghai Institute of Technical Physics, Chinese Academy of Sciences, Shanghai 200083, China

Correspondence should be addressed to Fangyu Yue; yuefy.mbi@gmail.com

Received 11 March 2014; Accepted 11 March 2014; Published 31 March 2014

Copyright © 2014 Fangyu Yue et al. This is an open access article distributed under the Creative Commons Attribution License, which permits unrestricted use, distribution, and reproduction in any medium, provided the original work is properly cited.

Advances in the growth, analysis, and characterization of various narrow-gap semiconductors and low-dimensional optoelectronic device structures have brought revolution into the modern day's information and communication technology including optical communication and computing systems. The main objective of this special issue is to include the recent advances in the experimental and theoretical research related to the growth, transport, and infrared properties of narrow-gap semiconductors and the fabrication, characterization, analysis, and simulation of various low-dimensional devices including quantum and nanostructures using narrow-gap semiconductors for optoelectronic applications. The basic aim of this special issue is to bring together in one publication the outstanding papers reporting new and original theoretical, experimental, and/or simulation works in the areas related to the narrow-gap semiconductors and low-dimensional structures.

Among a large number of submissions received from various researchers, we have selected only 7 papers for publication in this special issue. The work reported by H. Cui et al. is believed to be very useful in understanding the effects of metal-semiconductor contacts on the transient photovoltaic characteristics of HgCdTe-based photovoltaic arrays by using ultrafast lasers. In another paper, H. Cui et al. have analyzed the electrical modulation properties of the output intensity of two-photon absorption (TPA) pumping in HgCdTe photodiodes, which could be interesting for controlling a steady

output intensity of TPA by adjusting electric field in HgCdTe-based photodetectors. Both papers of H. Cui et al. are highly important for the design, fabrication, and characterization of HgCdTe-based infrared photodetectors. The paper of D. P. Samajdar and S. Dhar reports a mathematical model for investigating the valence band structure of alloy systems $\text{InAs}_{1-x}\text{Bi}_x$ and $\text{InSb}_{1-x}\text{Bi}_x$ by using the concept of valence-band anticrossing technique. The theoretical results for band structure of $\text{InAs}_{1-x}\text{Bi}_x$ and $\text{InSb}_{1-x}\text{Bi}_x$ could be of immense importance for the designing of diluted Bi-doped narrow-gap InAs- and InSb-based mid-/long-wavelength optoelectronic devices. A two-dimensional simulation for the effects of donor-like surface traps on two-dimensional electron gas (2DEG) and drain current collapse of AlGaIn/GaN high electron mobility transistors (HEMTs) has been investigated in detail by C. Yu et al. The paper of C. Zheng et al. reports the effects of same temperature GaN cap layer thickness on the quality of the InGaIn quantum well material and the well/barrier interface of InGaIn/GaN multiquantum-well based green light-emitting diodes grown on silicon substrates by MOCVD method. An interesting work on the phosphorescence of molecularly doped LEDs with blended polymer host and wide emission spectra reported by J. Wang et al. has also been considered for publication. The paper by R. Zhou et al. presents a detailed investigation on the second-harmonic generation (SHG), sum frequency generation (SFG), and difference frequency generation (DFG) from gold film with

a periodic subwavelength air nanohole patterns by means of the three-dimension (3D) finite-difference time-domain (FDTD) algorithm, revealing the second-order nonlinearity in triangular lattice perforated gold film due to surface plasmas resonance.

The guest editors have tried their best to select only a few papers out of many covering both the theoretical and experimental state-of-the-art research in the area of this special issue. It is believed that this special issue will be of significant interests to the scientists and researchers working in the areas related to the narrow band gap semiconductors and low-dimensional optoelectronic structures.

Acknowledgment

We would like to thank all the authors who submitted their papers to this special issue. The guest editors would also like to thank all the supporting staff of the publication house associated with the *Scientific World Journal* for their efforts to make the publication of this special issue possible.

Fangyu Yue
Satyabrata Jit
Weida Hu

Research Article

Second-Order Nonlinearity in Triangular Lattice Perforated Gold Film due to Surface Plasmas Resonance

Renlong Zhou,¹ Xiaoshuang Chen,² Yingyi Xiao,¹ Bingju Zhou,¹ Lingxi Wu,¹ Xiaojuan Liu,¹ Yongyi Gao,¹ and Jie Zhan¹

¹ School of Physics and Electronic Science, Hunan University of Science and Technology, Xiangtan 411201, China

² National Laboratory for Infrared Physics, Shanghai Institute of Technical Physics, Chinese Academy of Sciences, Shanghai 200083, China

Correspondence should be addressed to Renlong Zhou; rlzhou@mail.sitp.ac.cn and Xiaoshuang Chen; xschen@mail.sitp.ac.cn

Received 25 October 2013; Accepted 4 December 2013; Published 16 February 2014

Academic Editors: W. Hu, S. Jit, and F. Yue

Copyright © 2014 Renlong Zhou et al. This is an open access article distributed under the Creative Commons Attribution License, which permits unrestricted use, distribution, and reproduction in any medium, provided the original work is properly cited.

We have studied the excitation second-order nonlinearity through a triangular lattice perforated gold film instead of square lattice in many papers. Under the excitation of surface plasmas resonance effect, the second order nonlinearity exists in the noncentrosymmetric split-ring resonators arrays. Reflection of fundamental frequency wave through a triangular lattice perforated gold film is obtained. We also described the second harmonic conversion efficiencies in the second order nonlinear optical process with the spectra. Moreover, the electric field distributions of fundamental frequency above the gold film region are calculated. The light propagation through the holes results in the enhancement of the second order nonlinearity including second harmonic generation as well as the sum (difference) frequency generation.

1. Introduction

Nonlinear optical responses have been subject of intensive studies due to the development of nanofabrication techniques [1–6]. Second harmonic generation (SHG) is a powerful tool for probing physical and structure properties of the interface and surface of materials [7–12]. The SHG in square lattice with different structures, such as double-hole arrays or semiconductor nanoparticles arrays, has also been well studied [12, 13]. The underlying physical mechanism of SHG in metal nanoparticles has been explored numerically and experimentally [14–18]. The plasmonic oscillations of the conduction electrons inside the metal can induce the localized surface plasmon (SP) resonances. These localized surface plasmon (SP) resonances play important role in the process of nonlinear optical responses. The SHG from different SP resonance configurations such as split-ring resonators [17, 18], sharp metal tips [19, 20], metallodielectric multilayer structures [21], imperfect spheres [22, 23], and L-shaped and T-shaped

nanoparticles [9, 24–26] has been investigated. The theory of second harmonic generation (SHG) in three-dimensional structures consisting of arbitrary distributions of metallic spheres made of centrosymmetric materials is developed by means of multiple scattering of electromagnetic multipole fields [27]. Other theoretical methods with various kinds of approaches for the SHG have been developed by using the finite difference time domain (FDTD) method [13].

In this work, we present the surface plasmas excitation of the SHG in three-dimensional triangular lattice structures consisting of noncentrosymmetric split-ring resonators. We obtained the reflection spectra of fundamental frequency wave through a triangular lattice structures consisting of split-ring resonators. We also described the SH conversion efficiencies in the second-order nonlinear optical process with the spectra of second harmonic generation field. We find that the SH conversion efficiencies of SHG signal are in the range of about 10^{-12} – 10^{-14} . The electric field distributions of fundamental frequency and second harmonic are also

calculated by FDTD simulation. We have investigated the second-harmonic generation (SHG), sum frequency generation (SFG), and difference frequency generation (DFG). The enhanced SP resonance causes the increase of local second-order nonlinearity.

2. Theory and Method

Second-order nonlinearity of split-ring resonators nanostructures has been studied with the classical theoretical method in [13]. We consider the three-dimensional triangular lattice structures consisting of gold split-ring resonators.

The permittivity $\epsilon_r(\omega)$ of the gold split-ring resonators has the form

$$\epsilon_r(\omega) = 1 - \frac{\omega_p^2}{\omega(\omega + i\gamma)}. \quad (1)$$

The γ is collision frequency, and $\omega_p = \sqrt{e^2 n_0 / m_e \epsilon_0}$ is the plasma frequency of gold. The plasma frequency and collision frequency are taken as $\omega_p = 1.367 \times 10^{16} \text{ s}^{-1}$ and $\gamma = 6.478 \times 10^{13} \text{ s}^{-1}$, respectively.

There are two computational loops for the calculations of the fundamental and second harmonic fields in the FDTD program. The FDTD method to calculate the first-order field at the fundamental frequency has been discussed in [13]. The FDTD approach is also applied for the numerical calculation of the second-order equations. If we consider the second-order nonlinearity of the gold, the electric and magnetic field can be obtained as follows:

$$\begin{aligned} \frac{\partial B^{(2)}}{\partial t} &= -\nabla \times E^{(2)}, & \frac{\partial E^{(2)}}{\partial t} &= c^2 \nabla \times B^{(2)} - \frac{1}{\epsilon_0} j^{(2)}, \\ j^{(2)} &= -i\omega p^{(2)} = -i\omega \epsilon_0 (\epsilon_r - 1) E^{(2)} + S^{(2)}, \\ \frac{\partial j^{(2)}}{\partial t} &= -\gamma j^{(2)} + \frac{e^2 n_0}{m_e} E^{(2)} + S^{(2)}, \\ S^{(2)} &= \sum_k \frac{\partial}{\partial r_k} \left(\frac{j^{(1)} j^{(1)}_k}{e n_0} \right) \\ &\quad - \frac{e}{m_e} \left[\epsilon_0 (\nabla \cdot E^{(1)}) E^{(1)} + j^{(1)} \times B^{(1)} \right]. \end{aligned} \quad (2)$$

Here, k represents the x , y , and z coordinates. $J^{(1)}$ and $J^{(2)}$ represent the current density vectors of fundamental and harmonic waves, respectively. $E^{(1)}$ and $E^{(2)}$, $B^{(1)}$, and $B^{(2)}$ are the electric field and magnetic flux intensity vectors of fundamental and harmonic waves, respectively. n_0 is the ion density, m_e is the electron mass, and $S^{(2)}$ is the nonlinear source of the plasma for second-order nonlinearity, respectively.

The structure of a triangular lattice perforated gold film is shown in Figure 1. The perfectly matched absorbing boundary conditions are employed at the bottom and top of the computational space along the z direction, and the

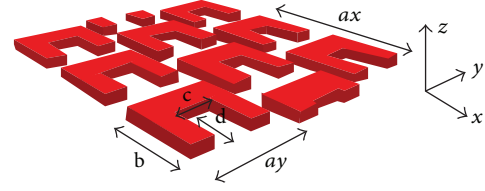


FIGURE 1: The structure of a triangular lattice structures consisting of gold split-ring resonators with the thickness $h = 30.5 \text{ nm}$ and the lattice periodic $a = ax = ay = 305 \text{ nm}$. There is the unit cell shape with $b = 219 \text{ nm}$, $c = 131 \text{ nm}$ and $d = 97 \text{ nm}$. The input light wave is polarized along the y direction and propagates along the z direction.

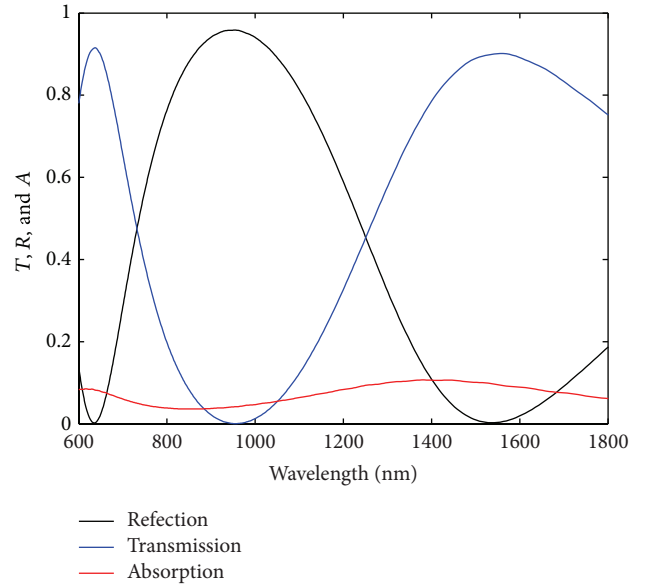


FIGURE 2: Reflection (transmission and absorption) spectra of fundamental frequency wave through a triangular lattice perforated gold film.

periodic boundary conditions are used on the boundaries of x and y directions. The incident wave is polarized along the y direction and propagates along the z -axis. The triangular lattice structure consists of split-ring resonators with the thickness $h = 30.5 \text{ nm}$ and the lattice periodic $a = ax = ay = 305 \text{ nm}$. The unit cell shape of split-ring resonator has $b = 219 \text{ nm}$, $c = 131 \text{ nm}$, and $d = 97 \text{ nm}$. The input light wave is polarized along the y direction and propagates along the z direction.

3. Results and Discussions

First, the normalized reflection (transmission and absorption) spectra of fundamental frequency wave through a triangular lattice perforated gold film are investigated here, and the calculation results are shown in Figure 2. There are two different SP resonance modes at the wavelengths 636 nm and 1548 nm for reflection spectra. These localized SP resonances at the wavelengths 636 nm and 1548 nm play important role in the process of nonlinear optical responses.

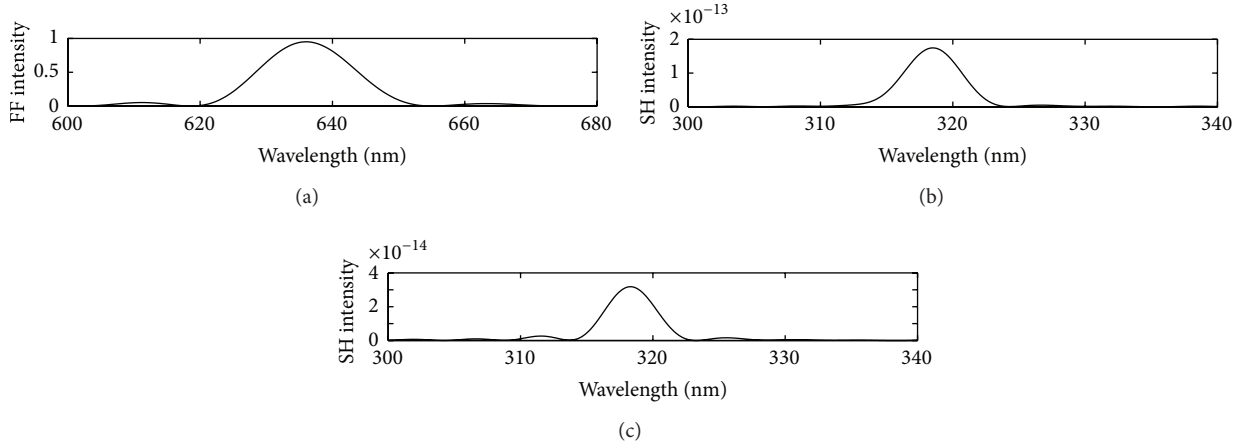


FIGURE 3: (a) The FTS for $E_y^{(1)}$ component of fundamental frequency field at the wavelength 636 nm. The FTS for (b) $E_x^{(2)}$ and (c) $E_y^{(2)}$ component of second-harmonic generation at the wavelength 318 nm.

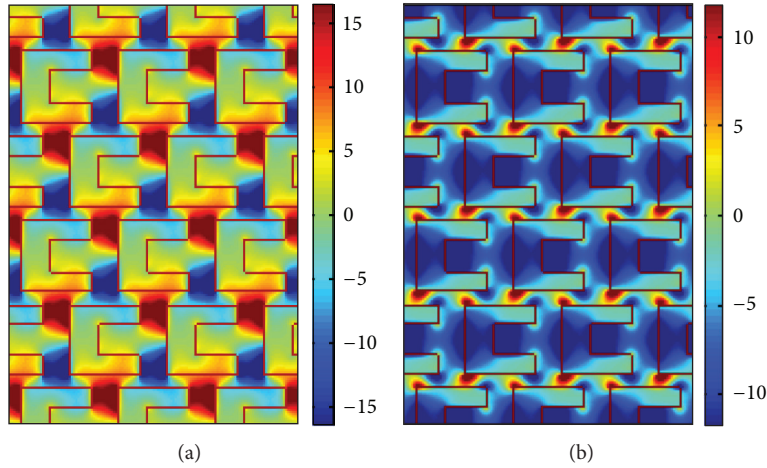


FIGURE 4: The electric field (a) $E_x^{(1)}$ and (b) $E_y^{(1)}$ distribution of fundamental frequency above the gold film region at wavelength 636 nm, respectively.

The nonlinear optical responses from different SP resonance in split-ring resonators can result as different second-order nonlinearity.

To obtain the SHG with a triangular lattice perforated gold film patterns, the input light wave $E_y^{(1)}$ is polarized along the y direction with wavelengths λ_1 or λ_2 :

$$E_y^{(1)} = E_0 \sin\left(\frac{2\pi ct}{\lambda_{1,2}}\right), \quad (3)$$

where E_0 is amplitude. We consider the wavelengths $\lambda_1 = 636$ nm or $\lambda_2 = 1548$ nm in (3) in order to satisfy the transmission of the fundamental frequency waves, respectively.

When the continuous wave $E_y^{(1)}$ at wavelength $\lambda_1 = 636$ nm is incident through the triangular lattice perforated gold film, one can see Fourier transform spectrum (FTS) of fundamental frequency wave at the wavelength 636 nm

in Figure 3(a). The FTS of the $E_x^{(2)}$ and the $E_y^{(2)}$ component of SHG at the wavelength 318 nm in Figures 3(b)-3(c), respectively, are also shown. To describe the SH conversion efficiencies in the second-order nonlinear optical process, the normalized SH intensity is defined as follows:

$$\eta = \left| \frac{E^{(2)}(2\omega_0)}{E^{(1)}(\omega_0)} \right|^2, \quad (4)$$

where ω_0 is the frequency of the incident FF wave. The x-polarized SH conversion efficiencies are about 10^{-13} while the y-polarized SH conversion efficiencies are about 10^{-14} for the fundamental frequency wave at the wavelength 636 nm as shown in Figures 3(b)-3(c). The electric field distributions of $E_x^{(1)}$ and $E_y^{(1)}$ for fundamental frequency field above the gold film region at wavelengths 636 nm are also shown in Figures 4(a)-4(b), respectively.

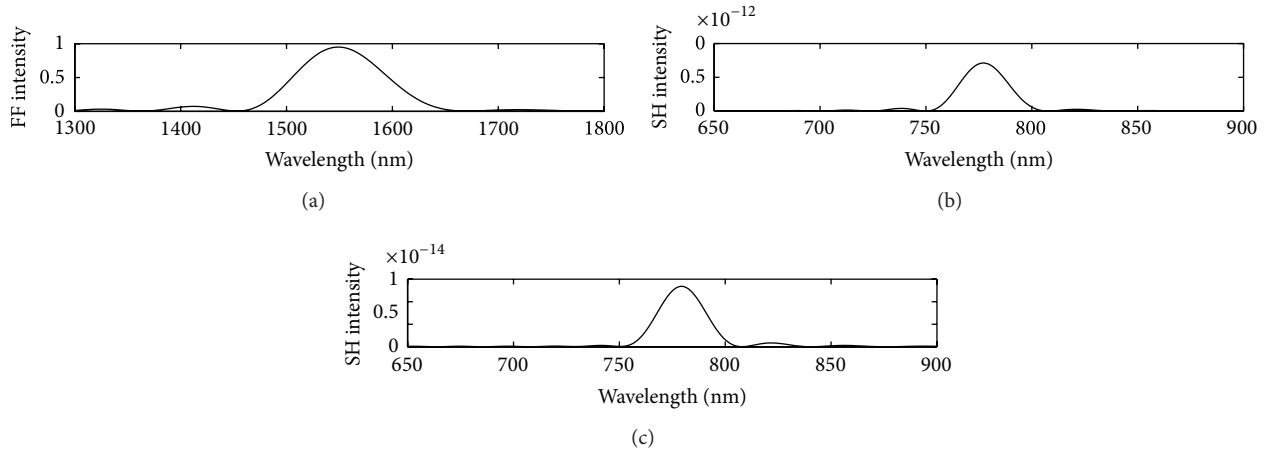


FIGURE 5: (a) The FTS for $E_y^{(1)}$ component of fundamental frequency wave at the wavelength 1548 nm. The FTS for (b) $E_x^{(2)}$ and (c) $E_y^{(2)}$ component of second-harmonic generation at the wavelength 774 nm.

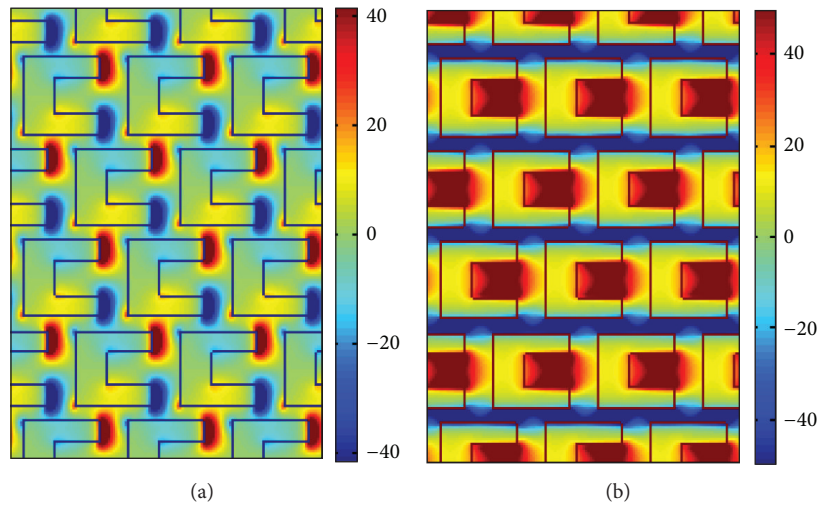


FIGURE 6: The electric field (a) $E_x^{(1)}$ and (b) $E_y^{(1)}$ distribution of fundamental frequency above the gold film region at wavelength 1548 nm, respectively.

When the continuous wave $E_y^{(1)}$ at wavelengths $\lambda_1 = 1548$ nm is incident through the triangular lattice perforated gold film, one can see FTS of fundamental frequency wave at the wavelength 1548 nm in Figure 5(a). The FTS of the $E_x^{(2)}$ and the $E_y^{(2)}$ component of SHG at the wavelength 774 nm in Figures 5(b)-5(c), respectively, are also shown. The x -polarized SH conversion efficiencies are about 10^{-12} while the y -polarized SH conversion efficiencies are about 10^{-14} for the fundamental frequency wave at the wavelength 1548 nm as shown in Figures 5(b)-5(c). The electric field distribution of E_x and E_y for fundamental frequency field above the gold film region at wavelengths 1548 nm is also shown in Figures 6(a)-6(b), respectively.

To obtain the second-order nonlinearity including second-harmonic generation as well as the sum (difference) frequency generation of the triangular lattice gold film with split-ring resonators patterns, the input light wave

$E_y^{(1)}$ is polarized along the y direction with two different wavelengths λ_1 and λ_2

$$E_y^{(1)} = E_0 \sin\left(\frac{2\pi c t}{\lambda_1}\right) + E_0 \sin\left(\frac{2\pi c t}{\lambda_2}\right), \quad (5)$$

where E_0 is amplitude. We consider two wavelengths $\lambda_1 = 636$ nm and $\lambda_2 = 1548$ nm in (5).

When the continuous wave $E_y^{(1)}$ with two different wavelengths 636 nm and 1548 nm is incident through the triangular lattice perforated gold film, it is found that there are four peaks for second-order nonlinearity at the wavelengths 318 nm, 451 nm, 774 nm, and 1080 nm in Figure 7, respectively. The second-order nonlinearity modes at wavelengths 318 nm and 774 nm are obtained from the SP modes of two

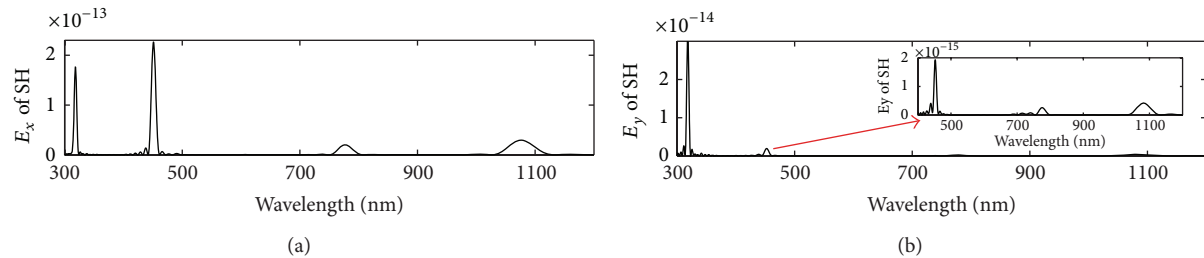


FIGURE 7: The FTS of second-order nonlinearity signals at the wavelength 318 nm, 451 nm, 774 nm, and 1080 nm for the two continuous wave $E_y^{(1)}$ incidence at the wavelengths $\lambda_1 = 636$ nm and $\lambda_2 = 1548$ nm, respectively.

incident continuous waves with wavelengths 636 nm and 1548 nm due to the SHG effect, respectively. The second-order nonlinearity mode at wavelengths 451 nm is the sum frequency field signals for two incident continuous waves with wavelengths 636 nm and 1548 nm. And the SH conversion efficiencies of sum-frequency field signal for two fundamental frequency wave incidence is about 10^{-13} or 10^{-14} . The second-order nonlinearity mode at wavelength 1080 nm is the difference frequency field for two incident continuous waves with wavelengths 636 nm and 1548 nm. The transmission of the fundamental light results from an enhancement of the local field. The strong local SP resonance induces an increase of the four second-order nonlinearity signals. The enhancement of the second-order nonlinearity signals include second-harmonic generation as well as the sum (difference) frequency generation.

4. Conclusions

Unlike SGH in square lattice perforated gold film in many papers, we have studied the excitation of second-order nonlinearity signals through a triangular lattice perforated gold film due to surface plasmas resonance effect. Based on the FDTD method, the SH conversion efficiencies in the second-order nonlinear optical process are studied. The electric field distributions of fundamental frequency are calculated. The second-order nonlinearity phenomenon including second-harmonic generation as well as the sum (difference) frequency generation is shown in our paper.

Conflict of Interests

The authors declare that there is no conflict of interests regarding the publication of this paper.

Acknowledgments

This work was supported by the National Natural Science Foundation of China under Grants 11247003 and 51175172. The authors would especially like to thank Dr. Yong Zeng for the discussion of FDTD simulations.

References

- [1] U. Kreibig and M. Vollmer, *Optical Properties of Metal Clusters*, Springer, Berlin, Germany, 1995.
- [2] T. F. Heinz, *Nonlinear Surface Electromagnetic Phenomena*, edited by H. E. Ponath and G. I. Stegeman, chapter 5, North-Holland, Amsterdam, The Netherlands, 1991.
- [3] H. Wang, E. Yan, E. Borguet, and K. B. Eisenthal, "Second harmonic generation from the surface of centrosymmetric particles in bulk solution," *Chemical Physics Letters*, vol. 259, no. 1-2, pp. 15–20, 1996.
- [4] J. I. Dadap, J. Shan, K. B. Eisenthal, and T. F. Heinz, "Second-harmonic Rayleigh scattering from a sphere of centrosymmetric material," *Physical Review Letters*, vol. 83, no. 20, pp. 4045–4048, 1999.
- [5] G. Gonella and H.-L. Dai, "Determination of adsorption geometry on spherical particles from nonlinear Mie theory analysis of surface second harmonic generation," *Physical Review B*, vol. 84, no. 12, Article ID 121402, 5 pages, 2011.
- [6] J. I. Dadap, J. Shan, and T. E. Heinz, "Theory of optical second-harmonic generation from a sphere of centrosymmetric material: small-particle limit," *Journal of the Optical Society of America B*, vol. 21, no. 7, pp. 1328–1347, 2004.
- [7] L. Wang, W. Hu, J. Wang et al., "Plasmon resonant excitation in grating-gated AlN barrier transistors at terahertz frequency," *Applied Physics Letters*, vol. 100, no. 12, Article ID 123501, 2012.
- [8] D. Hu, L. Wang, X. S. Chen et al., "Room-temperature plasmonic resonant absorption for grating-gate GaN HEMTs in far infrared terahertz domain," *Optical and Quantum Electronics*, vol. 45, no. 7, pp. 713–720, 2013.
- [9] G. Li, X. Chen, B. Ni et al., "Fractal H-shaped plasmonic nanocavity," *Nanotechnology*, vol. 24, no. 20, Article ID 205702, 2013.
- [10] G. Li, X. Chen, O. Li et al., "A novel plasmonic resonance sensor based on an infrared perfect absorber," *Journal of Physics D*, vol. 45, no. 20, Article ID 205102, 2012.
- [11] J. U. Fürst, D. V. Strekalov, D. Elser et al., "Naturally phase-matched second-harmonic generation in a whispering-gallery-mode resonator," *Physical Review Letters*, vol. 104, no. 15, Article ID 153901, 2010.
- [12] J. Butet, G. Bachelier, I. Russier-Antoine, C. Jonin, E. Benichou, and P.-F. Brevet, "Interference between selected dipoles and octupoles in the optical second-harmonic generation from spherical gold nanoparticles," *Physical Review Letters*, vol. 105, no. 7, Article ID 077401, 2010.

- [13] Y. Zeng, W. Hoyer, J. Liu, S. W. Koch, and J. V. Moloney, "Classical theory for second-harmonic generation from metallic nanoparticles," *Physical Review B*, vol. 79, no. 23, Article ID 235109, 2009.
- [14] C. M. Soukoulis, S. Linden, and M. Wegener, "Physics. Negative refractive index at optical wavelengths," *Science*, vol. 315, no. 5808, pp. 47–49, 2007.
- [15] V. M. Shalaev, "Optical negative-index metamaterials," *Nature Photonics*, vol. 1, no. 1, pp. 41–48, 2007.
- [16] J. Valentine, S. Zhang, T. Zentgraf et al., "Three-dimensional optical metamaterial with a negative refractive index," *Nature*, vol. 455, no. 7211, pp. 376–379, 2008.
- [17] M. W. Klein, C. Enkrich, M. Wegener, and S. Linden, "Second-harmonic generation from magnetic metamaterials," *Science*, vol. 313, no. 5786, pp. 502–504, 2006.
- [18] M. W. Klein, M. Wegener, N. Feth, and S. Linden, "Experiments on second- and third-harmonic generation from magnetic metamaterials," *Optics Express*, vol. 15, no. 8, pp. 5238–5247, 2007.
- [19] Y. Zeng and J. V. Moloney, "Volume electric dipole origin of second-harmonic generation from metallic membrane with none centro symmetric patterns," *Optics Letters*, vol. 34, no. 18, pp. 2844–2846, 2009.
- [20] C. C. Neacsu, G. A. Reider, and M. B. Raschke, "Second-harmonic generation from nanoscopic metal tips: symmetry selection rules for single asymmetric nanostructures," *Physical Review B*, vol. 71, no. 20, Article ID 201402, 2005.
- [21] M. C. Larciprete, A. Belardini, M. G. Cappeddu et al., "Second-harmonic generation from metallodielectric multilayer photonic-band-gap structures," *Physical Review A*, vol. 77, no. 1, Article ID 013809, 2008.
- [22] J. Shan, J. I. Dadap, I. Stiopkin, G. A. Reider, and T. F. Heinz, "Experimental study of optical second-harmonic scattering from spherical nanoparticles," *Physical Review A*, vol. 73, no. 2, Article ID 023819, 2006.
- [23] J. Nappa, G. Revillod, I. Russier-Antoine, E. Benichou, C. Jonin, and P. F. Brevet, "Electric dipole origin of the second harmonic generation of small metallic particles," *Physical Review B*, vol. 71, no. 16, Article ID 165407, 2005.
- [24] S. Kujala, B. K. Canfield, M. Kauranen, Y. Svirko, and J. Turunen, "Multipolar analysis of second-harmonic radiation from gold nanoparticles," *Optics Express*, vol. 16, no. 22, pp. 17196–17208, 2008.
- [25] H. Husu, B. K. Canfield, J. Laukkanen et al., "Chiral coupling in gold nanodimers," *Applied Physics Letters*, vol. 93, no. 18, Article ID 183115, 2008.
- [26] B. K. Canfield, H. Husu, J. Laukkanen et al., "Local field asymmetry drives second-harmonic generation in noncentrosymmetric nanodimers," *Nano Letters*, vol. 7, no. 5, pp. 1251–1255, 2007.
- [27] J. Xu and X. Zhang, "Second harmonic generation in three-dimensional structures based on homogeneous centrosymmetric metallic spheres," *Optics Express*, vol. 20, no. 2, pp. 1668–1684, 2012.

Research Article

Valence Band Structure of $\text{InAs}_{1-x}\text{Bi}_x$ and $\text{InSb}_{1-x}\text{Bi}_x$ Alloy Semiconductors Calculated Using Valence Band Anticrossing Model

D. P. Samajdar¹ and S. Dhar²

¹ Department of Electronics and Communication Engineering, Heritage Institute of Technology, Chowbaga Road, Anandapur, Kolkata 700107, India

² Department of Electronic Science, University of Calcutta, 92, A. P. C. Road, Kolkata 700009, India

Correspondence should be addressed to S. Dhar; sdhar_25@yahoo.co.in

Received 25 October 2013; Accepted 24 November 2013; Published 29 January 2014

Academic Editors: W. Hu, S. Jit, and F. Yue

Copyright © 2014 D. P. Samajdar and S. Dhar. This is an open access article distributed under the Creative Commons Attribution License, which permits unrestricted use, distribution, and reproduction in any medium, provided the original work is properly cited.

The valence band anticrossing model has been used to calculate the heavy/light hole and spin-orbit split-off energies in $\text{InAs}_{1-x}\text{Bi}_x$ and $\text{InSb}_{1-x}\text{Bi}_x$ alloy systems. It is found that both the heavy/light hole, and spin-orbit split E_+ levels move upwards in energy with an increase in Bi content in the alloy, whereas the split E_- energy for the holes shows a reverse trend. The model is also used to calculate the reduction of band gap energy with an increase in Bi mole fraction. The calculated values of band gap variation agree well with the available experimental data.

1. Introduction

Bi-containing III-V semiconductors are receiving great amount of interest in the last few years owing to their potential application in optoelectronic devices operating in the near to long infrared wavelength regions with enhanced capability. These materials are obtained by incorporating a small amount of Bi in the host semiconductor resulting in a major reduction in the material band gap. A comprehensive review of the state of the art in these materials has been provided in a recently published monogram [1]. Alloys, such as, GaAsBi, InGaAsBi, GaSbBi, InAsBi, and InSbBi, are being investigated for various target applications. The narrow band gaps $\text{InSb}_{1-x}\text{Bi}_x$ and $\text{InAs}_{1-x}\text{Bi}_x$ have been mostly investigated for applications in infrared detectors operating in the 3–5 and 8–12 μm spectral range [2] though the large miscibility gap and very low equilibrium solid solubility of Bi in the host semiconductors present certain difficulties in their growth [3]. Presence of Bi is also reported to reduce the dependence of the energy band gap of the alloys with temperature [4] which makes it possible to fabricate laser diodes with temperature insensitive emission wavelengths

[5]. In case of the well-investigated dilute III-V nitride alloys, the interaction of the N related resonant state with the conduction band of the host semiconductor causes the reduction in band gap. However, in III-V bismide alloys, the band gap reduction occurs due to a restructuring of the valence band as a result of the interaction of the Bi impurity level with the same band [6]. This interaction produces a splitting of both the heavy hole and the light hole energy bands into E_+ and E_- energy levels where the split E_+ level moves up in energy resulting in the observed band gap reduction. The valence band anticrossing (VBAC) model [7] has been successfully used to explain the behavior of III-V bismide materials. In this work, we have used this model to calculate the valence band structure of the narrow band gap semiconductors $\text{InAs}_{1-x}\text{Bi}_x$ and $\text{InSb}_{1-x}\text{Bi}_x$.

2. Mathematical Model

A theoretical model was used earlier to describe the restructuring of valence bands in the bismuth containing III-V semiconductors using $\mathbf{k}\cdot\mathbf{p}$ formalism [7]. The interaction

of the impurity bismuth atoms with the valence band of the corresponding host semiconductor was described by a 12×12 Hamiltonian which included 6 p-like states of the semiconductor lattice atom and the 6 localized p-like states of the added impurity atoms [8]. At the Γ point, where $\mathbf{k} = 0$, the 12×12 matrix can be written as:

$$H_0 = \begin{pmatrix} H & 0 & 0 & 0 & 0 & 0 & V & 0 & 0 & 0 & 0 & 0 \\ 0 & L & 0 & 0 & 0 & 0 & 0 & V & 0 & 0 & 0 & 0 \\ 0 & 0 & L & 0 & 0 & 0 & 0 & 0 & V & 0 & 0 & 0 \\ 0 & 0 & 0 & H & 0 & 0 & 0 & 0 & 0 & V & 0 & 0 \\ 0 & 0 & 0 & 0 & S & 0 & 0 & 0 & 0 & 0 & V & 0 \\ 0 & 0 & 0 & 0 & 0 & S & 0 & 0 & 0 & 0 & 0 & V \\ V & 0 & 0 & 0 & 0 & 0 & E_{\text{Bi}} & 0 & 0 & 0 & 0 & 0 \\ 0 & V & 0 & 0 & 0 & 0 & 0 & E_{\text{Bi}} & 0 & 0 & 0 & 0 \\ 0 & 0 & V & 0 & 0 & 0 & 0 & 0 & E_{\text{Bi}} & 0 & 0 & 0 \\ 0 & 0 & 0 & V & 0 & 0 & 0 & 0 & 0 & E_{\text{Bi}} & 0 & 0 \\ 0 & 0 & 0 & 0 & V & 0 & 0 & 0 & 0 & 0 & E_{\text{Bi-SO}} & 0 \\ 0 & 0 & 0 & 0 & 0 & V & 0 & 0 & 0 & 0 & 0 & E_{\text{Bi-SO}} \end{pmatrix}. \quad (1)$$

Here H , S , and V are given as [7]

$$\begin{aligned} H &= L = \Delta E_{\text{VBM}}x, \\ S &= \frac{1}{2}(L + H) - \Delta_0 - \Delta E_{\text{SO}}x, \\ V &= C_{\text{Bi}}\sqrt{x}. \end{aligned} \quad (2)$$

In the above equations, ΔE_{VBM} and ΔE_{SO} , respectively, denote the difference in valence-band maximum and spin-orbit split-off band energies between the end point compounds and x is the mole fraction of bismuth incorporated into the semiconductor alloy. Δ_0 gives the value of the split-off energy gap of the host semiconductor which for InAs, InSb, and GaSb are 0.39 eV, 0.81 eV, and 0.76 eV, respectively [9]. V is the matrix element describing the coupling between the host valence band and the Bi related impurity level and C_{Bi} is the coupling parameter which is used as a fitting parameter in our model [10]. E_{Bi} denotes the position of the heavy/light hole levels of the impurity atoms and $E_{\text{Bi-SO}}$ gives the corresponding spin-orbit split-off level [7].

The solution of the 12×12 matrix H_0 yields four distinct eigen values corresponding to the heavy/light hole E_+ and E_- energy levels and the spin-orbit-split off energy levels $E_{\text{SO}+}$ and $E_{\text{SO}-}$. Hence the 12×12 Hamiltonian reduces to a 4×4 matrix given by

$$H_R = \begin{pmatrix} L/H & 0 & V & 0 \\ 0 & S & 0 & V \\ V & 0 & E_{\text{Bi}} & 0 \\ 0 & V & 0 & E_{\text{Bi-SO}} \end{pmatrix}. \quad (3)$$

On solving the above matrix, we get the relations for the four distinct energy levels as explained by the VBAC model and are given as

$$\begin{aligned} E_{\text{HH/LH}\pm} &= \frac{1}{2} \left(L + E_{\text{Bi}} \pm \sqrt{L^2 - 2LE_{\text{Bi}} + E_{\text{Bi}}^2 + 4V^2} \right), \\ E_{\text{SO}\pm} &= \frac{1}{2} \left(S + E_{\text{Bi-SO}} \pm \sqrt{S^2 - 2SE_{\text{Bi-SO}} + E_{\text{Bi-SO}}^2 + 4V^2} \right). \end{aligned} \quad (4)$$

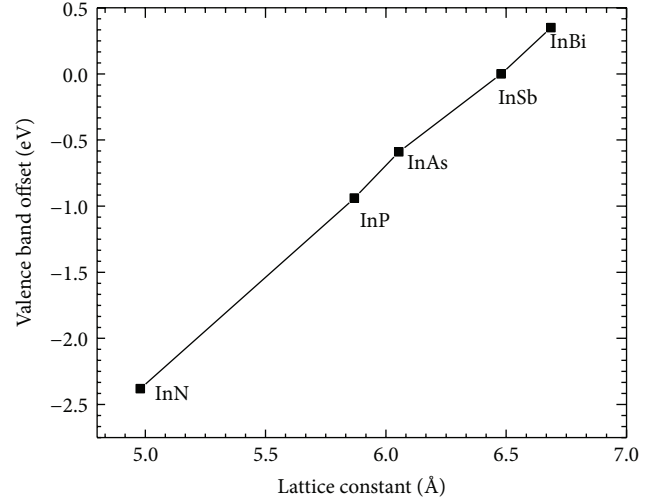


FIGURE 1: Plot of valence band offset versus lattice constant for In-containing III-V binaries. The values of VBO and lattice constants for these compounds are obtained from [9].

3. Valence Band Structure for $\text{InAs}_{1-x}\text{Bi}_x$

For VBAC calculations, we have considered Type I band alignment between InAs and InBi. The theoretically calculated band gap of InBi, as predicted by quantum dielectric theory by Barnett [11] is -1.62 eV. The valence band offset for InBi is found out to be 0.35 eV from Figure 1 (drawn by using the data from [9]) corresponding to its lattice constant of 6.686 Å [12]. The valence band offset ΔE_{VBM} between the end point compounds in $\text{InAs}_{1-x}\text{Bi}_x$ is obtained as 0.94 eV from an extrapolation of the variation of valence band offsets with lattice constants in Figure 1.

The value of the spin-orbit splitting energy for InBi is reported as 2.2 eV [12]. Hence the values of the valence band offset, conduction band offset, and spin-orbit split-off band offset for the end point compounds InAs and InBi are found out to be 0.94 eV, -1.03 eV, and -0.87 eV, respectively. Using the value of the atomic spin-orbit splitting energy for Bi of 1.5 eV [7], the position of the heavy/light hole levels for Bi, denoted by E_{Bi} , is found to be located 0.4 eV below the valence band maximum (VBM) of InAs [5] and the location of corresponding spin-orbit split-off level $E_{\text{Bi-SO}}$ is 1.9 eV below the VBM of InAs. The theoretical band gap of the ternary semiconductor is defined as the difference in energy between the VBAC calculated valence-band maximum and conduction band minimum obtained from the virtual crystal approximation (VCA) calculations, $E_{\text{CB-VCA}}$, which can be written as [7]

$$E_{\text{CB-VCA}} = E_g - \Delta E_{\text{CBM}}x \quad (5)$$

E_g is the band gap of InAs and $\Delta E_{\text{CBM}} = 1.03$ eV is the conduction band edge offset between InAs and InBi. In $\text{InAs}_{1-x}\text{Bi}_x$, the reported band gap reduction is 55 meV per 1 at % of Bi in the host semiconductor [12]. Using this value, we have calculated the value of the fitting parameter C_{Bi} to be 1.26 eV.

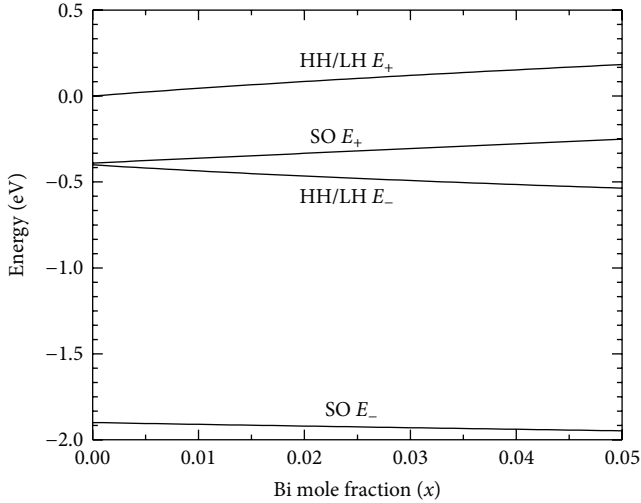


FIGURE 2: Position of the E_+ and E_- related heavy/light hole and spin-orbit split-off bands as a function of Bi mole fraction for $\text{InAs}_{1-x}\text{Bi}_x$, calculated using VBAC model.

Figure 2 shows the valence band structure of $\text{InAs}_{1-x}\text{Bi}_x$ as a function of Bi mole fraction x . The positions of the energy levels are calculated using (4). It can be noted from the figure that a repulsion exists between the E_+ and E_- levels corresponding to the heavy hole/light hole bands and the spin-orbit split-off energy bands. Both the heavy hole and the light hole E_+ levels are found to move up by about 45 meV for 1 at % Bi in the material with a corresponding downward movement of the E_- level. In the spin-orbit split-off band, the $E_{\text{SO}+}$ level moves up by about 28 meV per at % Bi. The upward movement of the E_+ level is mostly responsible for the band gap reduction in III-V bismides. Figure 3 gives the variation of band gap as a function of Bi mole fraction calculated using relation (5) and VBAC. Satisfactory agreement of the theoretical prediction with available experimental values is shown in the figure.

4. Valence Band Structure for $\text{InSb}_{1-x}\text{Bi}_x$

The valence band anticrossing interaction in $\text{InSb}_{1-x}\text{Bi}_x$ can be modelled by considering a valence band offset of 0.59 eV between InSb and InAs as can be observed from Figure 1. Thus, assuming the constancy of the localized impurity levels relative to the vacuum level, the Bi related impurity level E_{Bi} is located 1.0 eV below the VBM of InSb, whereas the corresponding spin-orbit split-off band is located at a depth of 2.5 eV below the VBM of InSb. The values of ΔE_{VBM} , ΔE_{CBM} , and ΔE_{SO} are found in a way similar to that for $\text{InAs}_{1-x}\text{Bi}_x$. The value of ΔE_{VBM} obtained from Figure 1 is 0.35 eV. Using this value and the value of energy gap for InBi, the value of ΔE_{CBM} is found out to be -1.44 eV and the value for ΔE_{SO} is -1.04 eV. The value of the fitting parameter C_{Bi} is calculated as 0.33 eV using experimentally obtained band gap reduction of 19 meV per at % of Bi in InSbBi [13].

Figure 4 presents the variation of the heavy/light hole and the spin-orbit split-off bands as a function of Bi mole

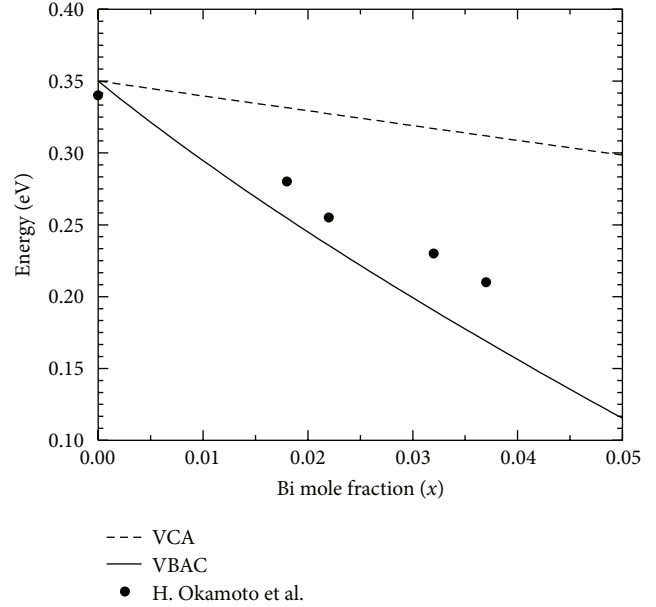


FIGURE 3: Theoretically calculated band gap of InAsBi as a function of Bi mole fraction using VCA and VBAC model. Experimental values of band gap are taken from [3].

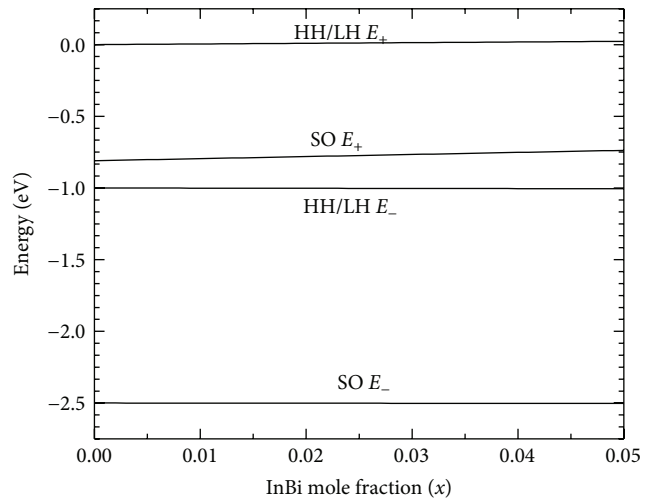


FIGURE 4: Calculated values of the E_+ and E_- related heavy/light hole, and the spin-orbit split bands in $\text{InSb}_{1-x}\text{Bi}_x$, as a function of Bi mole fraction x .

fraction x for $\text{InSb}_{1-x}\text{Bi}_x$. Here the E_+ level moves up by 4.6 meV for each at % Bi in the alloy, whereas the $E_{\text{SO}+}$ level increases by 14.5 meV for the same amount of Bi. These values are smaller as compared to those for $\text{InAs}_{1-x}\text{Bi}_x$ due to the larger separation between the E_+ and E_- levels and the SO_+ and SO_- levels. This occurs due to the fact that the Bi related impurity level E_{Bi} and the spin-orbit split-off level $E_{\text{Bi-SO}}$ are located at a greater depth from the VBM of InSb than in InAs which reduces the interaction between the coupled bands. Figure 5 shows the reduction in band gap with the increase in Bi mole fraction calculated using VBAC and VCA model.

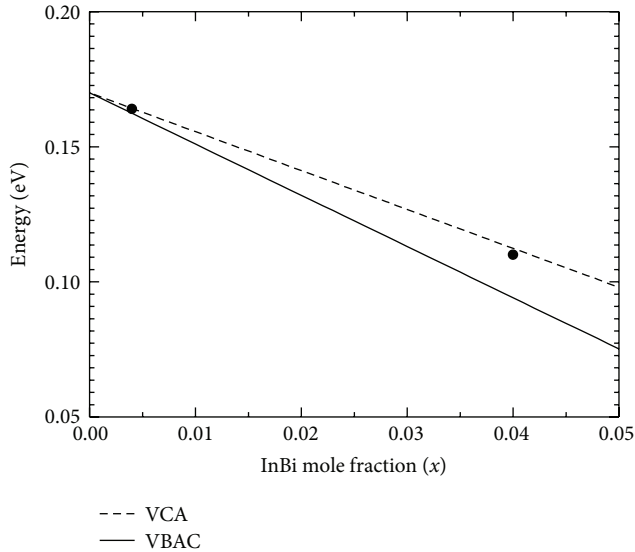


FIGURE 5: Band gap of InSbBi as a function of Bi mole fraction x calculated using VCA and VBAC model. The experimental points (solid dots) are from [14, 15].

A good agreement of this plot with experimental values is also presented in the same figure.

5. Conclusions

Valence band anticrossing model has been used to explore the valence band structures of Bi-containing alloys InAsBi and InSbBi. The theoretical results of band gap reduction agree fairly with the experimental data. The upward shift in the heavy/light hole E_+ level and spin-orbit split-off level E_{SO+} is observed in both cases. This upward movement of the heavy hole/light hole E_+ band is primarily responsible for the band gap reduction in these Bi-containing alloys.

Conflict of Interests

The authors declare that there is no conflict of interests regarding the publication of this paper.

Acknowledgments

The work was supported by the “University with Potential for Excellence” scheme of the University of Calcutta. One of the authors (D. P. Samajdar) is indebted to Heritage Institute of Technology for providing encouragement to carry on this work. The authors are also thankful to Dr. T. D. Das for his assistance in this work.

References

[1] H. Li and Z. M. Wang, Eds., *Bismuth-Containing Compounds*, vol. 186 of *Springer Series in Materials Science*, Springer Science, New York, NY, USA, 2013.

[2] H. Okamoto and K. Oe, “Growth of metastable alloy InAsBi by low-pressure MOVPE,” *Japanese Journal of Applied Physics*, vol. 37, no. 3, pp. 1608–1613, 1998.

[3] H. Okamoto and K. Oe, “Structural and energy-gap characterization of metalorganic-vapor-phase-epitaxy-grown InAsBi,” *Japanese Journal of Applied Physics*, vol. 38, no. 2 B, pp. 1022–1025, 1999.

[4] J. Yoshida, T. Kita, O. Wada, and K. Oe, “Temperature dependence of $\text{GaAs}_{1-x}\text{Bi}_x$ band gap studied by photoreflectance spectroscopy,” *Japanese Journal of Applied Physics*, vol. 42, no. 2, pp. 371–374, 2003.

[5] K. Oe, “Characteristics of semiconductor alloy $\text{GaAs}_{1-x}\text{Bi}_x$,” *Japanese Journal of Applied Physics*, vol. 41, no. 5, pp. 2801–2806, 2002.

[6] K. Alberi, O. D. Dubon, W. Walukiewicz, K. M. Yu, K. Bertulis, and A. Krotkus, “Valence band anticrossing in $\text{GaBi}_x\text{As}_{1-x}$,” *Applied Physics Letters*, vol. 91, no. 5, Article ID 051909, 2007.

[7] K. Alberi, J. Wu, W. Walukiewicz et al., “Valence-band anticrossing in mismatched III–V semiconductor alloys,” *Physical Review B*, vol. 75, no. 4, Article ID 045203, 2007.

[8] R. People and S. K. Sputz, “Band nonparabolicities in lattice-mismatch-strained bulk semiconductor layers,” *Physical Review B*, vol. 41, no. 12, pp. 8431–8439, 1990.

[9] I. Vurgaftman, J. R. Meyer, and L. R. Ram-Mohan, “Band parameters for III–V compound semiconductors and their alloys,” *Journal of Applied Physics*, vol. 89, no. 11 I, pp. 5815–5875, 2001.

[10] P. H. Jefferson, T. D. Veal, L. F. J. Piper et al., “Band anticrossing in $\text{GaN}_x\text{Sb}_{1-x}$,” *Applied Physics Letters*, vol. 89, no. 11, Article ID 111921, 2006.

[11] S. A. Barnett, “Direct E_0 energy gaps of bismuth-containing III–V alloys predicted using quantum dielectric theory,” *Journal of Vacuum Science & Technology A*, vol. 5, p. 2845, 1987.

[12] P. Carrier and S.-H. Wei, “Calculated spin-orbit splitting of all diamondlike and zinc-blende semiconductors: effects of $p_{1/2}$ local orbitals and chemical trends,” *Physical Review B*, vol. 70, no. 3, Article ID 035212, 9 pages, 2004.

[13] K. Y. Ma, Z. M. Fang, R. M. Cohen, and G. B. Stringfellow, “Organometallic vapor-phase epitaxy growth and characterization of Bi-containing III/V alloys,” *Journal of Applied Physics*, vol. 68, no. 9, pp. 4586–4591, 1990.

[14] S. K. Das, T. D. Das, S. Dhar, M. De La Mare, and A. Krier, “Near infrared photoluminescence observed in dilute GaSbBi alloys grown by liquid phase epitaxy,” *Infrared Physics and Technology*, vol. 55, no. 1, pp. 156–160, 2012.

[15] J. J. Lee and M. Razeghi, “Exploration of InSbBi for uncooled long-wavelength infrared photodetectors,” *Opto-Electronics Review*, vol. 6, no. 1, pp. 25–36, 1998.

Research Article

Effect of Same-Temperature GaN Cap Layer on the InGaN/GaN Multiquantum Well of Green Light-Emitting Diode on Silicon Substrate

Changda Zheng, Li Wang, Chunlan Mo, Wenqing Fang, and Fengyi Jiang

National Engineering Technology Research Center for LED on Si Substrate, Nanchang University, Nanchang 330047, China

Correspondence should be addressed to Changda Zheng; zhengchangda@ncu.edu.cn

Received 25 October 2013; Accepted 24 November 2013

Academic Editors: W. Hu, S. Jit, and F. Yue

Copyright © 2013 Changda Zheng et al. This is an open access article distributed under the Creative Commons Attribution License, which permits unrestricted use, distribution, and reproduction in any medium, provided the original work is properly cited.

GaN green LED was grown on Si (111) substrate by MOCVD. To enhance the quality of InGaN/GaN MQWs, same-temperature (ST) GaN protection layers with different thickness of 8 Å, 15 Å, and 30 Å were induced after the InGaN quantum wells (QWs) layer. Results show that a relative thicker cap layer is benefit to get InGaN QWs with higher In percent at fixed well temperature and obtain better QW/QB interface. As the cap thickness increases, the indium distribution becomes homogeneous as verified by fluorescence microscope (FLM). The interface of MQWs turns to be abrupt from XRD analysis. The intensity of photoluminescence (PL) spectrum is increased and the FWHM becomes narrow.

1. Introduction

Although GaN-based blue/green LEDs have been commercially used in color digital display, liquid crystal display back-lighting, traffic lamps, vehicle lamps, and general lighting areas as the significant progress achieved in the material growth and device manufacture, on the way to widely substitute the incandescent and fluorescent lamps as the general lighting source, cost lowering and electricity to light convert efficiency improvement are still required for III-nitride LEDs [1, 2].

Generally estimated, substrates cost 25 to 35 percent of the LED chips. So, how to reduce the cost of substrates is one of the key tasks for researchers. Due to lack of high quality, inexpensive, and large size GaN single-crystal substrate, commercially used GaN LED structures are mostly grown either on sapphire or SiC substrates. But there still exists some deficiency for both substrates. For example; they both are relatively expensive (especially SiC substrates) and hard, which introduces great complexity and trouble to the device fabrication processes and ultimately improves the devices cost. Therefore, silicon is used by some researchers as substrate to grow GaN-based LEDs and reduce device cost for its low cost, availability of large size, high surface quality, high

conductivity, and well-established processing techniques [3–5]. Today GaN blue LEDs have already been grown on silicon substrate by several groups, which provide one of the low-cost solutions for solid state lighting [6–8].

Otherwise, the increase in efficiency and output of GaN LEDs is still required. The difficulty to grow high efficient LEDs is mainly due to the fundamental problem associated with the growth of InGaN/GaN MQWs [9, 10]. Especially for green LEDs, high-Indium content InGaN layers with good crystal quality are necessary [11–13]. Hence, on the one hand, InGaN QWs must be gained with homogeneous indium incorporation. On the other hand, InGaN MQWs with abrupt interface are also needed [14–16]. In this study, based on the successful growth of crack free GaN epilayer on silicon substrate [7], we researched the effect of cap layer thickness on the quality of the InGaN QW material and the well/barrier interface.

2. Experiment

The InGaN/GaN MQWs green LED structure (as shown in Figure 1) was grown on silicon (111) substrate by Thomas Swan $6 \times 2''$ MOCVD with close-coupled showerhead reactor. Before being loaded into reactor, silicon substrates

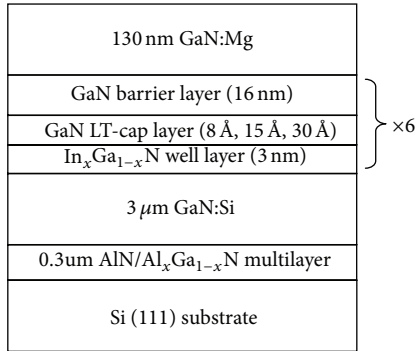


FIGURE 1: Epilayer structure of green InGaN/GaN light emitting diodes on silicon (111) substrate.

were degreased by $H_2SO_4 : H_2O_2 = 3 : 1$ mixture solution and etched with diluted HF (5%) solution to remove the surface contamination and oxide layer. After 30 minutes H_2 in situ heating at $1100^\circ C$ in reactor, only TMAI carried by H_2 was firstly injected into reactor for 2 minutes at about $800^\circ C$ to form a thin Al film on silicon surface and avoid silicon refused by metal gallium and/or nitrificated to SiN by ammonia (NH_3). A $0.3 \mu m$ AlN/Al_xGa_(1-x)N stress releasing layer and $3 \mu m$ GaN:Si layer were then grown. 200 nm InGaN strain prerelief layer and 6 periods InGaN/GaN MQWs were grown on *n*GaN. 130 nm GaN:Mg layer was lastly capped on the MQWs. For MQWs, every period was composed of InGaN well layer, GaN cap layer at well temperature, and GaN barrier layer at temperature $120^\circ C$ higher than well. The cap layers were designed with three thicknesses of 8 Å, 15 Å, and 30 Å and those samples were marked as sample "A," sample "B," and sample "C," respectively. Double crystal X-ray diffractometry (DCXRD) was used to characterize the structure quality of MQWs. Fluorescence microscope (FLM) was used to get fluorescence image of QWs under the optional excitation wavelength from 380 nm to 420 nm. The selected wavelength of dichroic mirror is 430 nm and barrier filter is 450 nm in this study. Photoluminescence (PL) spectrum was used to characterize the optical performance of InGaN/GaN MQWs excited with He-Ge 325 nm laser.

3. Results and Discussion

XRD Omega/2theta rocking scan was induced to check the quality of MQWs. The scan range is from -5000 arcsec to $+5000$ arcsec. The diffraction peak of GaN (0002) plan is set on the symmetry scanning center of the rocking curve and is located as 0 position of the *x*-coordinate. As shown in Figure 2, satellite peaks clearly observed for samples B and C on the left side of diffraction curves, indicating that fine QW/QB periodic structure and abrupt QW/QB interface are formed for MQW with 15 Å and 30 Å cap layer. 1st to 4th order satellite peaks are also appeared for these two samples. Still, it is found that 3rd and 4th order peaks widths of sample B are even larger compared with those of sample C, showing that sample B has relative worse QW/QB interface. Furthermore, when the cap thickness is reduced to 8 Å (Sample A), the satellite peaks become not easy to be distinguished from

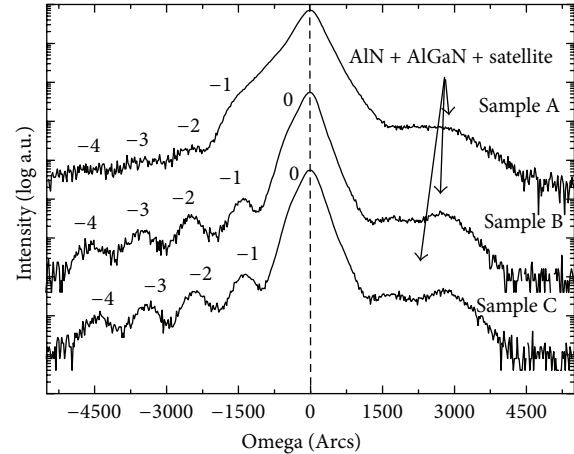


FIGURE 2: DCXRD Omega-2theta rocking curve on GaN (0002) plan for three samples. The center peak is defined as GaN (002) peak. InGaN diffraction peak is marked as zero order peak.

the left side of diffraction curve. This means that clear QW/QB periodic structure was not formed for the well being destroyed when temperature ramping from well to higher barrier temperature with only 8 Å thin cap layer. For samples B and C, an overall peak can be differentiate from the left of GaN (0002) peak, which is assigned to 0 order peak from the well In_xGa_(1-x)N (0002) diffraction. As the insufficiently resolution of the double crystal X-ray diffractionmeter, this peak is not so clearly and encapsulated in GaN (0002) peak. For sample A, no 0 order peak can be resolved from the curve. The reason may also be stem from the heat-damage effect and heterogeneous In fraction of QW for sample A. For all three samples, there are no clearly symmetric satellite peaks on the right side of the diffraction curves as which lies on the left side. One reason is that the X-ray intensity decreases as the diffraction angle increases. Another reason is that AlN and AlGaN multilayer was grown to release the stress between Si substrate and GaN layer and the multilayer diffraction peaks are also laid on the right of GaN (002) peak. These peaks superpose with MQWs satellite peak, which brings on an indecipherable overall peak.

The FLM images of the samples are showed in Figure 3. It is found that sample A has an uneven FL image. Extra-bright points are distributed on the picture. This is caused by the well InGaN decomposed and segregated when ramping to grow barrier and p-GaN at high temperature. For image of sample B, the uneven points become not so serious. No extremely bright points can be found from sample B. But some local uneven areas still exist on the image. When cap thickness increased to 30 Å, the image becomes more uniform and no big bright points appear on it. The FL images are usually used to reflect the Indian distribution in the well. It can be concluded that the MQWs have a much more uniform fluorescence microscope images as increasing the cap layer thickness. Thicker cap would protect the well from being decomposed. The results are also in accordance with the conclusions from XRD test.

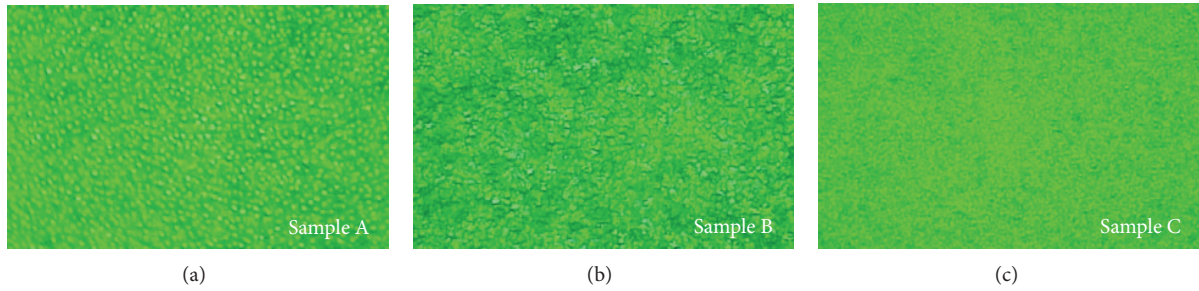


FIGURE 3: The FLM images for three samples. The selected wavelength of dichroic mirror is 430 nm and barrier filter is 450 nm in the test.

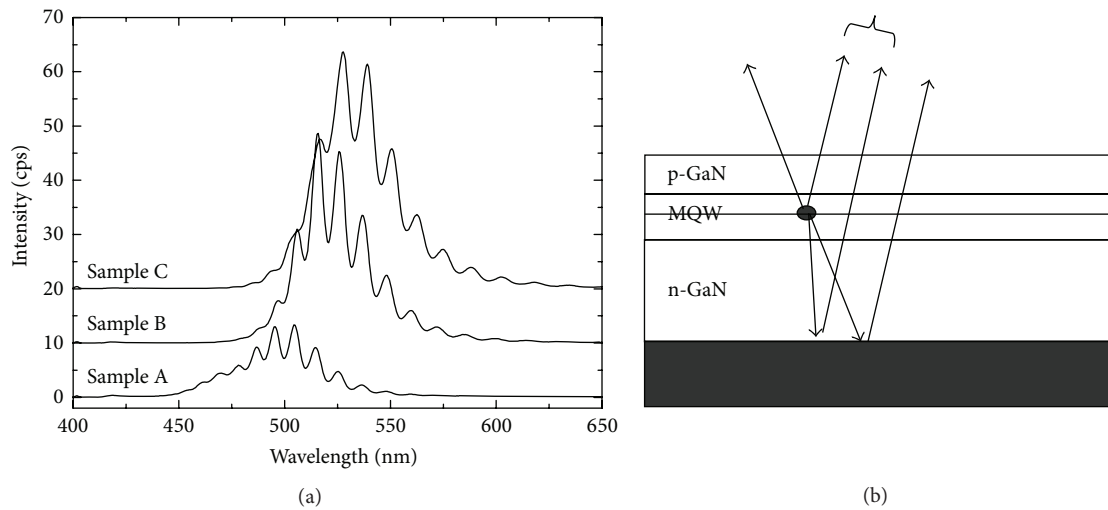


FIGURE 4: (a) PL spectra of the three samples are excited by He-Ge 325 nm laser at room temperature. (b) Schematic diagram of optical cavity effects of the MQWs light from the surface and GaN/Si interface reflection.

The lighting characteristic of MQWs was taken by photoluminescence (PL) measurement with He-Ge 325 nm laser as excited source. The PL spectra of three samples are shown in Figure 4(a). The peak wavelength is all loaded in green wavelength ranged from 500 nm to 535 nm. All the spectra are not smooth curve but have interference candy stripes accompanying with the curve. Those stripes are from optical cavity effects [17]. As shown in Figure 4(b), green light is generated from MQW excited by laser. Some fraction of light is directly extracted out the wafer surface. Some fraction of light is firstly reflected by GaN/Si interface and then extracted out the wafer surface. The two lights have optical path difference, forming regions of high and low intensities. As the cap increases from 8 Å to 30 Å, the intensity of the PL spectra increases and the peak wavelength is red-shifted from 500 nm to 530 nm. At the same time, the full width of half maximum (FWHM) of the spectra becomes narrow. This can also be explained by the well protection effect leading to increasing the In component and uniformity with the thicker cap layer.

4. Conclusions

In conclusion, GaN-based green LED structure with InGaN/GaN MQWs has been grown on Si (111) substrate by

MOCVD. InGaN QW was found to decompose at the higher temperature when growing GaN barrier and Mg-doped GaN:Mg layer, which results in heterogeneous indium component in InGaN QW-layer and poor InGaN/GaN interface. Same-temperature GaN cap layer after InGaN QW is effective in preventing the InGaN decomposition. As the cap thickness increases, the indium distributions become homogeneous as verified by FL. The interface of MQWs turns out to be abrupt from XRD analysis. The intensity of PL spectrum is increased and FWHM becomes narrow. Thus, the cap layer is one of the key optional tuning parameters to improve GaN-based green MQWs quality and further to obtain high-efficiency LEDs.

Acknowledgments

This work was supported by the National Natural Science Foundation of China (no. 51072076), by the National High Technology Research and Development program of China (no. 2011AA03A101 and no. 2012AA04I002), by the Fund for Less Developed Regions of the National Natural Science Foundation of China (Grant no. 11364034), by the Key Program of the National Natural Science Foundation of China (Grant no. 61334001), and the National Key Technology Research and Development Program of China (no. 2011BAE32B01).

References

- [1] E. F. Schubert and J. K. Kim, "Solid-state light sources getting smart," *Science*, vol. 308, no. 5726, pp. 1274–1278, 2005.
- [2] J. Cho, E. F. Schubert, and J. K. Kim, "Efficiency droop in light-emitting diodes: challenges and countermeasures," *Laser & Photonics Reviews*, vol. 7, pp. 408–421, 2013.
- [3] F. Schulze, A. Dadgar, J. Bläsing, A. Diez, and A. Krost, "Metalorganic vapor phase epitaxy grown InGaNGaN light-emitting diodes on Si(001) substrate," *Applied Physics Letters*, vol. 88, no. 12, Article ID 121114, 2006.
- [4] A. Dadgar, C. Hums, A. Diez, F. Schulze, J. Bläsing, and A. Krost, "Epitaxy of GaN LEDs on large substrates: Si or sapphire?" in *Proceedings of the Advanced LEDs for Solid State Lighting*, pp. 63550R–63558R, Gwangju, South Korea, September 2006.
- [5] C. Zheng, L. Wang, C. Mo et al., "Efficiency improvement of vertical structure GaN blue LEDs on Si(111) substrate by surface roughening," *Journal of Central South University of Technology*, vol. 142, pp. 127–130, 2007.
- [6] T. Chen, Y. Wang, P. Xiang et al., "Crack-free InGaN multiple quantum wells light-emitting diodes structures transferred from Si(111) substrate onto electroplating copper submount with embedded electrodes," *Applied Physics Letters*, vol. 100, Article ID 241112, 2012.
- [7] C. D. Zheng, C. L. Mo, W. Q. Fang, and F. Y. Jiang, "Effect of the conduction type of Si(111) substrates on the performance of GaN MQW LED epitaxial films," *Advanced Materials Research*, vol. 750, pp. 1029–1033, 2013.
- [8] C. Mo, W. Fang, Y. Pu, H. Liu, and F. Jiang, "Growth and characterization of InGaN blue LED structure on Si(111) by MOCVD," *Journal of Crystal Growth*, vol. 285, no. 3, pp. 312–317, 2005.
- [9] M. Senthil Kumar, J. Y. Park, Y. S. Lee, S. J. Chung, C.-H. Hong, and E.-K. Suh, "Effect of barrier growth temperature on morphological evolution of green InGaN/GaN multi-quantum well heterostructures," *Journal of Physics D*, vol. 40, no. 17, pp. 5050–5054, 2007.
- [10] S. J. Leem, Y. C. Shin, E. H. Kim et al., "Optimization of InGaN/GaN multiple quantum well layers by a two-step varied-barrier-growth temperature method," *Semiconductor Science and Technology*, vol. 23, no. 12, Article ID 125039, 2008.
- [11] T. Langer, A. Kruse, F. A. Ketzer et al., "Origin of the "green gap": increasing nonradiative recombination in indium-rich GaInN/GaN quantum well structures," *Physica Status Solidi (C)*, vol. 8, no. 7-8, pp. 2170–2172, 2011.
- [12] J.-C. Lee and Y.-F. Wu, "Thermal effect of multi-quantum barriers within InGaN/GaN multi-quantum well light-emitting diodes," *Thin Solid Films*, vol. 518, no. 24, pp. 7437–7440, 2010.
- [13] S.-N. Lee, H. S. Paek, J. K. Son et al., "Surface modifications and optical properties of blue InGaN single quantum well by in-situ thermal treatments," *Physica Status Solidi (C)*, vol. 4, no. 1, pp. 141–144, 2007.
- [14] Z. L. Li, P. T. Lai, and H. W. Choi, "A reliability study on green InGaN-GaN light-emitting diodes," *IEEE Photonics Technology Letters*, vol. 21, no. 19, pp. 1429–1431, 2009.
- [15] K. R. Kasarla, W. Chiang, R. Rahinu, and D. Korakakis, "Optimization of GaN barriers during the growth of InGaN/GaN quantum wells at low temperature," in *Proceedings of the Materials Research Society Symposium*, pp. 43–48, December 2008.
- [16] Y.-J. Lee, Y.-C. Chen, C.-J. Lee, C.-M. Cheng, S.-W. Chen, and T.-C. Lu, "Stable temperature characteristics and suppression of efficiency droop in InGaN green light-emitting diodes using pre-TMIn flow treatment," *IEEE Photonics Technology Letters*, vol. 22, no. 17, pp. 1279–1281, 2010.
- [17] Y. C. Shen, J. J. Wierer, M. R. Krames et al., "Optical cavity effects in InGaN/GaN quantum-well-heterostructure flip-chip light-emitting diodes," *Applied Physics Letters*, vol. 82, no. 14, pp. 2221–2223, 2003.

Research Article

Donor-Like Surface Traps on Two-Dimensional Electron Gas and Current Collapse of AlGa_N/Ga_N HEMTs

Chen-hui Yu,¹ Qing-zhou Luo,² Xiang-dong Luo,^{1,3} and Pei-sheng Liu¹

¹ Jiangsu Key Laboratory of ASIC Design, Nantong University, Nantong 226019, China

² School of Remote Sensing, Nanjing University of Information Science and Technology, Nanjing 210044, China

³ Key Laboratory of Nanodevices and Applications, Suzhou Institute of Nano-Tech and Nano-Bionics, Chinese Academy of Sciences, Suzhou 215123, China

Correspondence should be addressed to Chen-hui Yu; yichu@ntu.edu.cn

Received 27 July 2013; Accepted 12 August 2013

Academic Editors: W. Hu, S. Jit, and F. Yue

Copyright © 2013 Chen-hui Yu et al. This is an open access article distributed under the Creative Commons Attribution License, which permits unrestricted use, distribution, and reproduction in any medium, provided the original work is properly cited.

The effect of donor-like surface traps on two-dimensional electron gas (2DEG) and drain current collapse of AlGa_N/Ga_N high electron mobility transistors (HEMTs) has been investigated in detail. The depletion of 2DEG by the donor-like surface states is shown. The drain current collapse is found to be more sensitive to the addition of positive surface charges. Surface trap states with higher energy levels result in weaker current collapse and faster collapse process. By adopting an optimized backside doping scheme, the electron density of 2DEG has been improved greatly and the current collapse has been greatly eliminated. These results give reference to the improvement in device performance of AlGa_N/Ga_N HEMTs.

1. Introduction

Two-dimensional electron gas (2DEG) based AlGa_N/Ga_N high electron mobility transistors (HEMTs) have shown promising advantages in high-power, high-frequency, and high-temperature applications [1–4]. They have also demonstrated good properties in optoelectronic responses [5]. The drain current collapse effect in these devices is a serious obstacle at the present stage to further improve device performances [6–8]. Some efforts have been made to explore the mechanisms of drain current collapse, such as self-heating [9–11], trapping [3], and surface states [12–15]. The bulk traps in AlGa_N/Ga_N layers which absorb electrons from channels and virtual gate effects [12] which deplete the channel in the device by the accumulated negative charges in the surface have been found to be the main reason causing the reduction of 2DEG in channels [16]. However, the influence of donor-like surface traps on the drain current collapse has not been fully discussed. Donor-like traps mainly originate from shallow impurities, interface states, and surface states. They may interact with the negative charges in the surface which have a decisive influence on the 2DEG in the HEMT channels

[12–16]. The effects of donor-like surface traps with different energy levels and density have been ignored in previous work.

In this paper, we analyze these ignored effects in AlGa_N/Ga_N HEMTs with a two-dimensional device simulation method. We adopt the density of the surface charge as a measurement of the activities of surface traps, since filling or emptying charges on the surface from the traps can change the charge density on the surface directly and influence the response of the channel electrons to the voltage consequently. The sensitivity of current collapse to the variation of negative charges on the surface is firstly investigated for a better understanding of behavior of donor-like surface traps.

2. Method and Device Structure

Two-dimensional drift-diffusion simulations of the AlGa_N/Ga_N HEMTs are performed. Device structure of the AlGa_N/Ga_N HEMT is shown in Figure 1. The gate length is 0.7 μm and the opening spaces between the contacts are $L_{GD} = 0.7 \mu\text{m}$ and $L_{SG} = 2 \mu\text{m}$. The thickness of AlGa_N layer with composition of 35% aluminum is 29 nm. The mobilities of

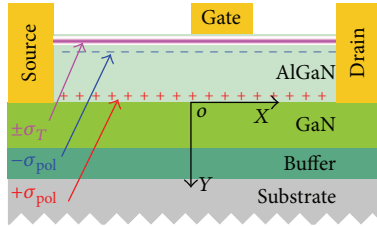


FIGURE 1: Cross-sectional structure of AlGaIn/GaN HEMT. Positive sheet charge $+\sigma_{pol}$ is caused by spontaneous polarization and piezoelectric effect. Equivalent negative sheet charge $-\sigma_{pol}$ is fixed on the AlGaIn surface. Surface trap states are represented with $\pm\sigma_T$.

electrons and holes in GaN layer are $100 \text{ cm}^2 \text{ V}^{-1} \text{ s}^{-1}$ and $30 \text{ cm}^2 \text{ V}^{-1} \text{ s}^{-1}$, respectively. The mobilities of electrons and holes in AlGaIn layer are $100 \text{ cm}^2 \text{ V}^{-1} \text{ s}^{-1}$ and $5 \text{ cm}^2 \text{ V}^{-1} \text{ s}^{-1}$, respectively [9, 17–21].

A positive sheet charge $+\sigma_{pol}$ caused by spontaneous polarization and piezoelectric effect [22–24] is fixed at the interface and the equivalent negative sheet charge $-\sigma_{pol}$ on the AlGaIn surface. The fixed sheet charge density is assumed to be $-1.15 \times 10^{13} \text{ cm}^{-2}$ on the AlGaIn surface and $1.15 \times 10^{13} \text{ cm}^{-2}$ at AlGaIn/GaN interface [25–27], respectively. Surface states σ_T are considered uniformly distributed on the regions between source and gate. When the surface states are taken into calculation, the initial charge density is modified by adding or removing static charges at the surface. The net charge density between the contacts is expressed as $\sigma_{net} = -\sigma_{pol} + \sigma_T$. A default temperature of 300 K is employed in simulations [28]. A transient voltage $V_{dd} = 6 \text{ V}$ is applied to the drain with maintaining gate bias $V_G = 0 \text{ V}$. The drain voltage is pulsed from 0.1 V to V_{dd} and the pulse time is adjusted in each case.

3. Results and Discussion

In Figure 2, the reduction of average electron density in the channel is shown as the surface charges, σ_T , change from 0 to $-5 \times 10^{12} \text{ cm}^{-2}$. The increase of negative charge density (NCD) on the surface leads to the depletion of 2DEG. This is mainly caused by the induced positive charges that appeared around the AlGaIn/GaN interface by NCD, which then neutralize the electrons in channel. Another point is the same increase of electron density near the gate along X direction as the previous increase of NCD. It provides clear evidence of the existence of a virtual gate in this device.

The electric field intensities in both X and Y direction as the surface charges, σ_T , change from 0 to $-5 \times 10^{12} \text{ cm}^{-2}$ are shown in Figure 3. The electric field intensity in X direction is cut at AlGaIn/GaN interface, $Y = 0 \text{ nm}$, and in Y direction is cut at $X = 0.25 \text{ nm}$, as shown in Figure 1. The electric field intensity in both X and Y directions decreases as the negative surface charge density is increased. The decrease of electric field intensity is consistent with the decrease of electron density in Figure 2 and produces positive consequences. Firstly, since the electric field intensity near the interface is reduced, the electrons in the channel cannot acquire

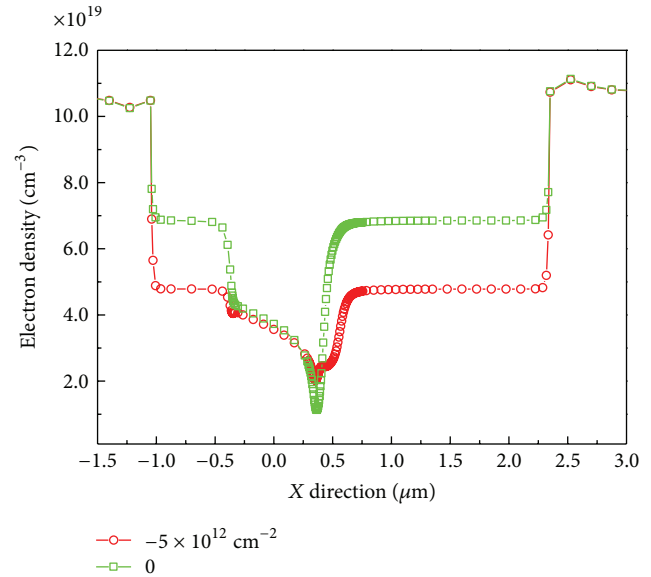


FIGURE 2: Electron density versus X direction cut at AlGaIn/GaN interface. A depletion of 2DEG in channel due to negative charges on the surface is shown.

high enough temperature, and the number of hot electrons reduces. Moreover, the addition of negative charges at surface makes surface potential lower and interface potential higher [28, 29], which in turn causes the electron affinity to increase. The higher electron affinity causes again the reduction of the amount of hot electrons. Secondly, the quantum tunneling effect is weakened with the increase of potential barrier and the decrease of electron energy [30]. The weakening of both hot electron and quantum tunneling effects prevents electrons escaping from the channel. Therefore, the increase of the negative charges on the surface is helpful in eliminating the drain current collapse.

The comparison of drain current collapse under different surface negative charges is shown in Figure 4 with a pulse time of 2 ms. One open circle is with $5 \times 10^{12} \text{ cm}^{-2}$ negative charges added at surface and another open square is with no negative charges. The peaks of the time-dependent drain current under different amount of surface negative charges are put together in order to have a better understanding of the decay process of drain current. We can see that the collapse of drain current in line (a) (with $-5 \times 10^{12} \text{ cm}^{-2}$ in the surface) is reduced because of the addition of negative charges at AlGaIn layer surface. The negative charges make the electrons more difficultly escape from the channel. Besides, the drain current in the line (a) takes less time to reach the steady state. In other words, the process of drain current collapse with more negative charges is accelerated.

The drain current response versus drain voltage under different amount of surface charges is shown in Figure 5. Taking case (a) as a standard example, cases (b) and (c) can be considered as added $3\sigma_{pol}$ positive charges and $3\sigma_{pol}$ negative charges on the surface of case (a), respectively. When the negative charge $-3\sigma_{pol}$ is added to the surface as case (c), the drain current does not decrease as much as the increase of the

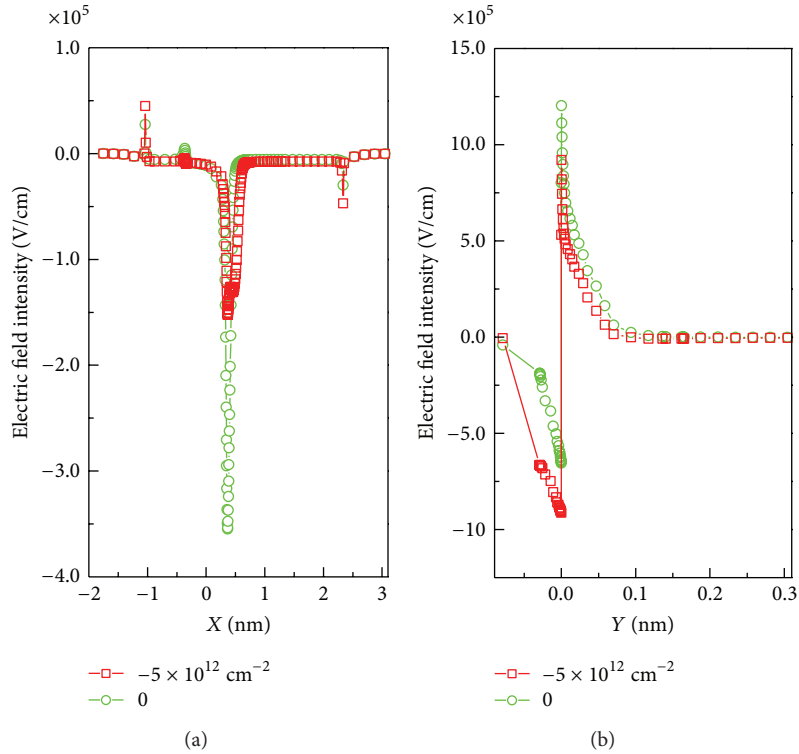


FIGURE 3: (a) Electric field intensity versus X direction. (b) Electric field intensity versus Y direction.

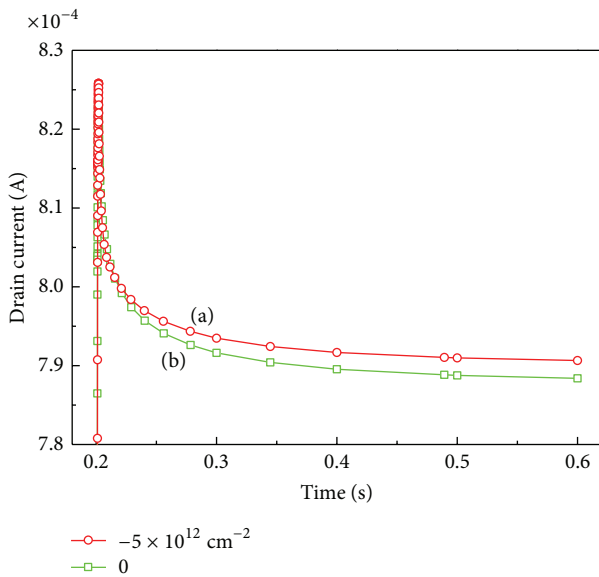


FIGURE 4: Comparison of drain current versus pulse time. The curves of drain current are shifted to hold two peaks together for better comparison.

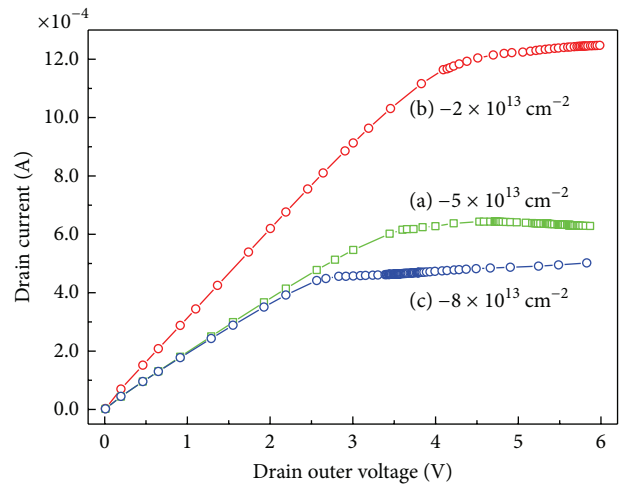


FIGURE 5: Drain current response versus drain voltage under different amount of surface charges.

drain current caused by the same amount of $+3\sigma_{pol}$ positive charge added at the surface as case (b). This result means that the transient drain current response to time of AlGaIn/GaN HEMTs is more sensitive to the presence of the positive charges rather than the negative charges. In the HEMT

device, the holes are the main origin of great difference in sensitivity to the charge changes at the surface. The free holes populate at the surface, and part of them is caused by the inner electric field because the inner electric field divides a couple of electrons and holes into two individual parts. Then, these holes come to the surface, and part of the holes gathers at the surface because they get to the surface to compensate the extra negative charge added in the surface and maintain the electric neutrality. Therefore, when the negative charges

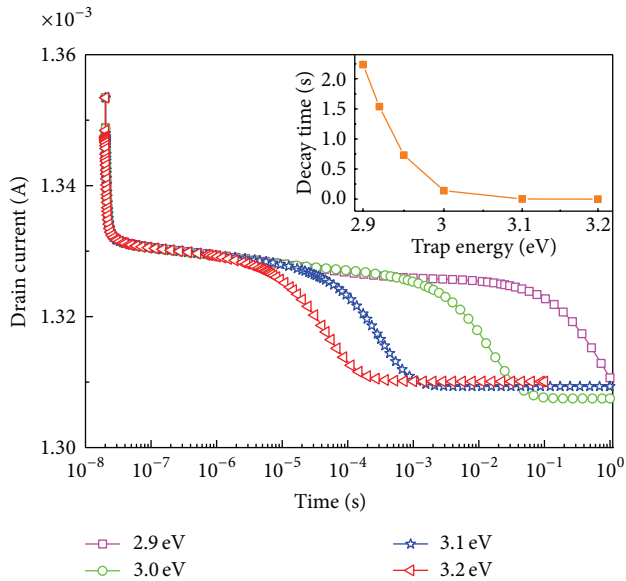


FIGURE 6: Drain current collapses at different energy levels. Inset is the curves of decay time to steady states.

are added at the surface, they do not reduce the drain current because some of them are neutralized by holes in the surfaces first.

Transient drain current responses versus time with $V_{gs} = 0$ V and a fixed trap density of $4 \times 10^{13} \text{ cm}^{-2}$ are shown in Figure 6. Transient voltages are applied to drains. The time for the voltage to turn on is about 10^{-8} s. The energy levels of the donor type traps are referenced to the edge of valence band and set to be 3.2 eV, 3.1 eV, 3.0 eV and 2.9 eV, respectively. For better comparison, the different peak values of the drain currents are hold together. A noticeable decrease in the decay value of drain current can be observed as the donor-like trap energy level goes higher. The increase of DTI (donor-like trap ionization) leads to the increase of number of positive charges accumulating in the surface. When the drain voltage jumps up from 0 V to 6 V, millions of electrons are injected into the drain electrode and then couple with these positive charges. This process causes the decrease of positive charge density (PCD). We can consider the decrease of PCD as addition of negative charges in the surface. From discussion above, we know that the addition of negative charges weakens not only the hot electron effects, but also the quantum tunneling effects. Therefore, the collapse amount is reduced as the energy level goes higher.

Meanwhile, the noticeable decrease in the decay time is also observed as the donor-like trap energy level goes higher. Higher energy level traps produce more positive charges and then these charges are neutralized by injected electrons. As more negative charges are added on the surface, depletion process is accelerated, and thus the transient drain current costs less time to reach the steady states. The decay time with different donor-like trap energies is shown in the inset. The decay time does not change linearly with the change in the energy level but decreases exponentially along with

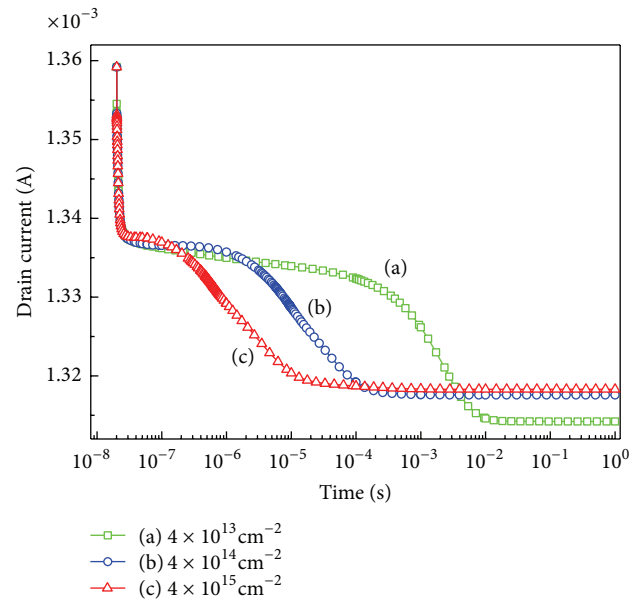


FIGURE 7: Drain current collapse at different trap density.

the increase in donor-like traps energy level. As the energy level becomes higher, the differences of decay times become smaller. This is also the result of change of surface charges. The higher energy levels cause more positive charges to populate at the surface and then these positive charges are partially captured by electrons. It means that more negative charges are added at the surface. Similar to the discussion above, the drain current response is not sensitive to the presence of the negative charges. Thus, after the appearance of more negative charges at the surface, the current collapse process is weakened.

The transient response at different values of trap density on the surface with a fixed trap energy level 3.1 eV is shown in Figure 7. The trap densities are considered with (a) $\sigma_T = 4 \times 10^{13} \text{ cm}^{-2}$, (b) $\sigma_T = 4 \times 10^{14} \text{ cm}^{-2}$, and (c) $\sigma_T = 4 \times 10^{15} \text{ cm}^{-2}$. The differences of decay time become smaller with increasing trap density. Similar to the explanation of Figure 6, it can be concluded that the variation of charge in the surface has great role in the current response. The trap density of (c), namely, $4 \times 10^{15} \text{ cm}^{-2}$, has the most positive charge density at the surface. After the voltage is shifted from 0.1 V to 6 V, the electrons injected from drain electrode are captured by the positive charges. The process causes negative charge density to be increased at the surface. Because the current response is less sensitive to the addition of negative charge density, the case (c) in which more negative charges are captured has less decay time compared to case (a).

To eliminate the negative influence of surface trap density on the surface, we suggest an optimizing scheme with backside doping [9, 29] to improve the performance of these HMETs. The total thickness of GaN layer is 75 nm, the bottom 35 nm is doped with phosphorus ($2 \times 10^{18} \text{ cm}^{-3}$). The GaN layer of 75 nm can restrict electron effectively. The doping of the bottom modulates the energy band structure [9] and thus not only prevents the electron going into the

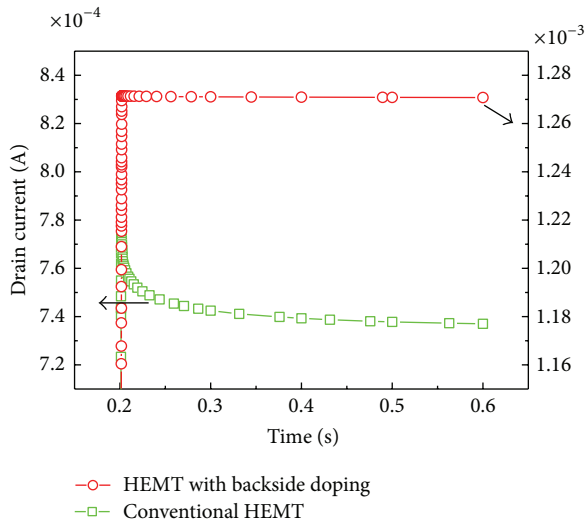


FIGURE 8: Comparison before and after backside doping.

bulk traps, but also makes a bigger potential well for holding more electrons. When considering the advantages of backside doping and the disadvantages of parasitic conductance, the doping concentration and the thickness of doping layer have to be optimized as previously reported work [9, 29]. Figure 8 shows the comparison of drain current collapse before and after backside doping. It can be seen that the drain current has been enhanced and the collapse in drain current has almost been eliminated. After introducing the backside doping, we can improve the electron density in the device and eliminate the drain current collapse effect greatly.

4. Conclusions

The effects of donor-like surface traps on current collapse of AlGaIn/GaN HEMTs have been systematically investigated. It is demonstrated that the negative charges have been neutralized by the positive charges on the surface. Thus, the current response is less sensitive to the presence of the negative charge. Based on the response of drain current, the ionization of donor type traps is thought to cause the reduction of decay time and the acceleration of decrease of drain current. The ionization process collects holes and then induces an increase in the number of negative charges gathering on the surface. Higher energy levels or larger density of donor type traps leads to the increase of ionization of donor type traps in the surface and subsequently causes the reduction of decay time and the weakening of current collapse amount. By adopting the backside doping in the bottom of GaN layer with 50 nm thickness, the energy band structure can be regulated and more electrons can be accumulated in the channel. Then, the collapse of drain current has been eliminated effectively. Our results are beneficial to the improvement of drain current in AlGaIn/GaN HEMTs.

Conflict of Interests

The authors of the paper, do not have a direct financial relation that might lead to a conflict of interests for any of them or regarding the publication of this paper.

Acknowledgments

This work was supported in part by the National Natural Science Foundation of China (Grant nos. 11104150, 11274330, and 41001288), the Natural Science Foundation of Jiangsu Province of China (Grant no. BK2010571), and the Open Project of Key Laboratory of Nanodevices and Applications (Grant no. 12ZD03).

References

- [1] A. Tarakji, G. Simin, N. Ilinskaya et al., "Mechanism of radio-frequency current collapse in GaN-AlGaIn field-effect transistors," *Applied Physics Letters*, vol. 78, no. 15, pp. 2169–2171, 2001.
- [2] G. Meneghesso, F. Rampazzo, P. Kordoš, G. Verzellesi, and E. Zanoni, "Current collapse and high-electric-field reliability of unpassivated GaN/AlGaIn/GaN HEMTs," *IEEE Transactions on Electron Devices*, vol. 53, no. 12, pp. 2932–2940, 2006.
- [3] X.-D. Wang, W.-D. Hu, X.-S. Chen, and W. Lu, "The study of self-heating and hot-electron effects for AlGaIn/GaN double-channel HEMTs," *IEEE Transactions on Electron Devices*, vol. 59, no. 5, pp. 1393–1401, 2012.
- [4] S. Keller, Y.-F. Wu, G. Parish et al., "Gallium nitride based high power heterojunction field effect transistors: process development and present status at UCSB," *IEEE Transactions on Electron Devices*, vol. 48, no. 3, pp. 552–559, 2001.
- [5] S. Schöche, J. Shi, A. Boosalis et al., "Terahertz optical-Hall effect characterization of two-dimensional electron gas properties in AlGaIn/GaN high electron mobility transistor structures," *Applied Physics Letters*, vol. 98, no. 9, Article ID 092103, 2011.
- [6] O. Mitrofanov and M. Manfra, "Dynamics of trapped charge in GaN/AlGaIn/GaN high electron mobility transistors grown by plasma-assisted molecular beam epitaxy," *Applied Physics Letters*, vol. 84, no. 3, pp. 422–424, 2004.
- [7] P. D. Ye, B. Yang, K. K. Ng et al., "GaN metal-oxide-semiconductor high-electron-mobility-transistor with atomic layer deposited Al₂O₃ as gate dielectric," *Applied Physics Letters*, vol. 86, no. 6, Article ID 063501, 2005.
- [8] E. Kohn, I. Daumiller, M. Kunze et al., "Transient characteristics of GaN-based heterostructure field-effect transistors," *IEEE Transactions on Microwave Theory and Techniques*, vol. 51, no. 2, pp. 634–642, 2003.
- [9] W. D. Hu, X. S. Chen, F. Yin, J. B. Zhang, and W. Lu, "Two-dimensional transient simulations of drain lag and current collapse in GaN-based high-electron-mobility transistors," *Journal of Applied Physics*, vol. 105, no. 8, Article ID 084502, 2009.
- [10] L. Wang, W. D. Hu, X. S. Chen, and W. Lu, "The role of ultrathin AlN barrier in the reduction in the hot electron and self-heating effects for GaN-based double-heterojunction high electron mobility transistors," *Journal of Applied Physics*, vol. 108, no. 5, Article ID 054501, 2010.

- [11] W. D. Hu, X. S. Chen, Z. J. Quan et al., "Simulation and optimization of GaN-based metal-oxide-semiconductor high-electron-mobility-transistor using field-dependent drift velocity model," *Journal of Applied Physics*, vol. 102, no. 3, Article ID 034502, 2007.
- [12] R. Vetury, N. Q. Zhang, S. Keller, and U. K. Mishra, "The impact of surface states on the DC and RF characteristics of AlGaIn/GaN HFETs," *IEEE Transactions on Electron Devices*, vol. 48, no. 3, pp. 560–566, 2001.
- [13] G. Meneghesso, G. Verzellesi, R. Pierobon et al., "Surface-related drain current dispersion effects in AlGaIn-GaN HEMTs," *IEEE Transactions on Electron Devices*, vol. 51, no. 10, pp. 1554–1561, 2004.
- [14] J. M. Tirado, J. L. Sánchez-Rojas, and J. I. Izpura, "Trapping effects in the transient response of AlGaIn/GaN HEMT devices," *IEEE Transactions on Electron Devices*, vol. 54, no. 3, pp. 410–417, 2007.
- [15] J. M. Tirado, J. L. Sanchez-Rojas, and J. I. Izpura, "2D simulation of static surface states in AlGaIn/GaN HEMT and GaN MESFET devices," *Semiconductor Science and Technology*, vol. 20, no. 8, pp. 864–869, 2005.
- [16] P. B. Klein, S. C. Binari, K. Ikossi-Anastasiou et al., "Investigation of traps producing current collapse in AlGaIn/GaN high electron mobility transistors," *Electronics Letters*, vol. 37, no. 10, pp. 661–662, 2001.
- [17] N. Braga, R. Mickevicius, R. Gaska, M. S. Shur, M. Asif Khan, and G. Simin, "Simulation of gate lag and current collapse in gallium nitride field-effect transistors," *Applied Physics Letters*, vol. 85, no. 20, pp. 4780–4782, 2004.
- [18] C. Nguyen, N. X. Nguyen, and D. E. Grider, "Drain current compression in GaN MODFETs under large-signal modulation at microwave frequencies," *Electronics Letters*, vol. 35, no. 16, pp. 1380–1382, 1999.
- [19] X. Hu, A. Koudymov, G. Simin et al., "Si₃N₄/AlGaIn/GaN-metal-insulator-semiconductor heterostructure field-effect transistors," *Applied Physics Letters*, vol. 79, no. 17, pp. 2832–2834, 2001.
- [20] G. Simin, A. Koudymov, A. Tarakji et al., "Induced strain mechanism of current collapse in AlGaIn/GaN heterostructure field-effect transistors," *Applied Physics Letters*, vol. 79, no. 16, pp. 2651–2653, 2001.
- [21] E. J. Miller, E. T. Yu, C. Poblentz, C. Elsass, and J. S. Speck, "Direct measurement of the polarization charge in AlGaIn/GaN heterostructures using capacitance-voltage carrier profiling," *Applied Physics Letters*, vol. 80, no. 19, pp. 3551–3553, 2002.
- [22] J.-P. Ao, D. Kikuta, N. Kubota, Y. Naoi, and Y. Ohno, "Copper gate AlGaIn/GaN HEMT with low gate leakage current," *IEEE Electron Device Letters*, vol. 24, no. 8, pp. 500–503, 2003.
- [23] X. Hu, J. Deng, N. Pala et al., "AlGaIn/GaN heterostructure field-effect transistors on single-crystal bulk AlN," *Applied Physics Letters*, vol. 82, no. 8, pp. 1299–1301, 2003.
- [24] W. D. Hu, X. S. Chen, Z. J. Quan, C. S. Xia, W. Lu, and P. D. Ye, "Self-heating simulation of GaN-based metal-oxide-semiconductor high-electron-mobility transistors including hot electron and quantum effects," *Journal of Applied Physics*, vol. 100, no. 7, Article ID 074501, 2006.
- [25] V. O. Turin and A. A. Balandin, "Performance degradation of GaN field-effect transistors due to thermal boundary resistance at GaN/substrate interface," *Electronics Letters*, vol. 40, no. 1, pp. 81–83, 2004.
- [26] A. Brannick, N. A. Zakhleniuk, B. K. Ridley, J. R. Shealy, W. J. Schaff, and L. F. Eastman, "Influence of field plate on the transient operation of the AlGaIn/GaN HEMT," *IEEE Electron Device Letters*, vol. 30, no. 5, pp. 436–438, 2009.
- [27] I. Daumiller, D. Theron, C. Gaquière et al., "Current instabilities in GaN-based devices," *IEEE Electron Device Letters*, vol. 22, no. 2, pp. 62–64, 2001.
- [28] L. Wang, W. D. Hu, X. S. Chen, and W. Lu, "Analysis of interface scattering in AlGaIn/GaN/InGaIn/GaN double-heterojunction high-electron-mobility transistors," *Journal of Electronic Materials*, vol. 41, no. 8, pp. 2130–2138, 2012.
- [29] Z. Y. Fan, J. Li, M. L. Nakarmi, J. Y. Lin, and H. X. Jiang, "AlGaIn/GaN/AlN quantum-well field-effect transistors with highly resistive AlN epilayers," *Applied Physics Letters*, vol. 88, no. 7, Article ID 073513, 2006.
- [30] W. D. Hu, X. S. Chen, Z. J. Quan, C. S. Xia, W. Lu, and H. J. Yuan, "Demonstration and dynamic analysis of trapping of hot electrons at gate edge model for current collapse and gate lag in GaN-based high-electron-mobility transistor including self-heating effect," *Applied Physics Letters*, vol. 89, no. 24, Article ID 243501, 2006.

Research Article

Phosphorescent Molecularly Doped Light-Emitting Diodes with Blended Polymer Host and Wide Emission Spectra

Jun Wang, Jun Gou, and Weizhi Li

State Key Lab of Electronic Thin Films and Integrated Devices, School of Optoelectronic Information, University of Electronic Science and Technology of China (UESTC), Chengdu 610054, China

Correspondence should be addressed to Jun Wang; uestc_wj@yahoo.com

Received 30 July 2013; Accepted 4 October 2013

Academic Editors: W. Hu and S. Jit

Copyright © 2013 Jun Wang et al. This is an open access article distributed under the Creative Commons Attribution License, which permits unrestricted use, distribution, and reproduction in any medium, provided the original work is properly cited.

Stable green light emission and high efficiency organic devices with three polymer layers were fabricated using bis[2-(4'-tert-butyl-phenyl)-1-phenyl-1H-benzimidazole-N,C^{2'}] iridium(III) (acetylacetonate) doped in blended host materials. The 1 wt% doping concentration showed maximum luminance of 7841 cd/cm² at 25.6 V and maximum current efficiency of 9.95 cd/A at 17.2 V. The electroluminescence spectra of devices indicated two main peaks at 522 nm and 554 nm coming from phosphor dye and a full width at half maximum (FWHM) of 116 nm. The characteristics of using blended host, doping iridium complex, emission spectrum, and power efficiency of organic devices were investigated.

1. Introduction

Organic light-emitting diodes (OLEDs) have attracted more and more attention for their various potential applications such as display, backlight for liquid crystal display, and next-generation light sources since Tang and Vanslyke reported the bright green OLEDs with sandwiched structure [1–3]. Most phosphorescent OLEDs (PhOLEDs) typically were made up of a thin light emitting layer sandwiched between electron and hole blocking layers as well as charge transport layers by means of high vacuum evaporation techniques [4, 5]. The use of these multilayer architectures by vacuum deposition is expected to pose a challenge in reducing device manufacturing costs and controlling the doping concentration precisely. In contrast, solution processing of polymer-based organic semiconductors offers the potential for fabrication of electronic devices at a significantly reduced cost. Whether by spin coating or by ink jet printing, a variety of efforts have enabled high performance OLEDs to be commercialized [6, 7]. Burroughes reported the polymer organic light emitting diodes (PLEDs) using poly(*p*-phenylene vinylene) (PPV) as emission layer between indium-tin oxide (ITO) anode and metal cathode [8]. Polyvinylcarbazol film doped with dyes of coumarin 6,

coumarin 47, and Nile red were used to fabricate PLED with ink-jet printing method by Hebner et al. [9]; the characteristics of the printing device were similar to the film with same composition deposited by spin coating method. Multicolor polymer light-emitting devices with solution processing have also been explored with cross-linked photochemically characteristic materials [10, 11].

But solution processed polymer light emitting devices are typically made up of not more than three layers, in which one of the layers performed the simultaneous tasks of charge transport and light emission [12]. Most of conjugated polymers typically indicate hole-only or electron-only transporting characteristic, which cause the unbalance holes and electrons in the emission layer. The unbalance charge within the device is unsuitable for improving power efficiency of PLEDs. Therefore, to achieve high efficiency PLEDs, several factors need to be considered, including the balance of electrons and holes, strong radiative transitions for singlet excitons, efficient light extraction, and developing phosphorescence emitters with triplet-triplet energy transfer characteristic.

Nonconjugated polymer poly(*N*-vinylcarbazole) (PVK) has been a commonly used polymer host for phosphorescent dyes [13–15]. But PVK has, however, an inherent defect in that

its electron and hole mobility difference are too large [16]. In contrast to PVK-hosted PLEDs, the performances of PFO-hosted PLEDs could be enhanced from the selective removal of the electron-transporting material during fabrication of the functional layer [17], so that using PVK as hole transporting layer and PFO blended host layer is more suitable for high efficiency polymer device.

In this study polymer organic devices with three polymer layers structure including hole injection layer, hole transporting layer, and emission layer were fabricated using iridium complex as emission material by solution process. The addition of injection layer was used to increase the device stability and hole injection. The emission layer consisted of phosphor dye and mixed polymer host which blended hole and electron transporting materials. High efficiency and wide emission spectra organic polymer devices with different doping concentrations were fabricated and characterized.

2. Experiments

The PLEDs fabrication was described as follows: substrates coated with indium tin oxide (ITO) were first cleaned with water and organic solvents and then underwent surface treatment involving oxygen plasma. This was followed by coating a 50 nm thick layer of poly(ethylene dioxythiophene): poly(styrene sulfonic acid) (PEDOT:PSS) spun on ITO films at 4000 rpm. And then 40 nm thick conductive polymer PVK acting as hole transporting layer was spun on the substrate surface. Next, blended host polymer with Ir(III) complex was spin-coated at room temperature under ambient conditions from a CHCl_3 solution, resulting in 80 nm thick films. The blended conductive polymer host, poly(9,9-di-n-octylfluorene-2,7-diyl) (PFO) + 30 wt% 2-(4-*tert*-butylphenyl)-5-(4-biphenyl)-1,3,4-oxadiazole (PBD), was obtained from a commercial supplier and was used as host material without purification. The phosphorescent dye bis[4-*tert*-butyl-1-phenyl-1H-benzimidazolato-*N,C*^{2'}] iridium(III) (acetylacetonate) [(tpbi)₂Ir(acac)] was synthesized in our lab and used to fabricate small molecular organic device with high efficiency [18]. Finally, a 4 nm thick Ba metal and 150-nm-thick aluminum cathode layer were deposited on the substrate in high vacuum environment through a shadow mask with 5 mm width openings. The devices thus obtained have a typical structure of ITO/PEDOT:PSS (50 nm)/PVK (40 nm)/PFO + 30 wt% PBD:(tpbi)₂Ir(acac) (*x*%) (80 nm)/Ba (4 nm)/Al (150 nm) (*x* = 1, 2, 4, and 8 for device A, B, C, and D, resp.).

The metal layer thicknesses were determined *in situ* by oscillating quartz thickness monitors and an ellipsometer for the evaporated and spin-coated films, respectively. EL spectra and Commission International De L'Eclairage (CIE) (1931) coordinates of the devices were measured with a PR650 spectroscan spectrometer. Luminance (*L*), current density (*J*), and bias voltage (*V*) characteristics were recorded simultaneously with the measurement of EL spectra by combining the spectrometer with a Keithley 2400 programmable voltage-current source.

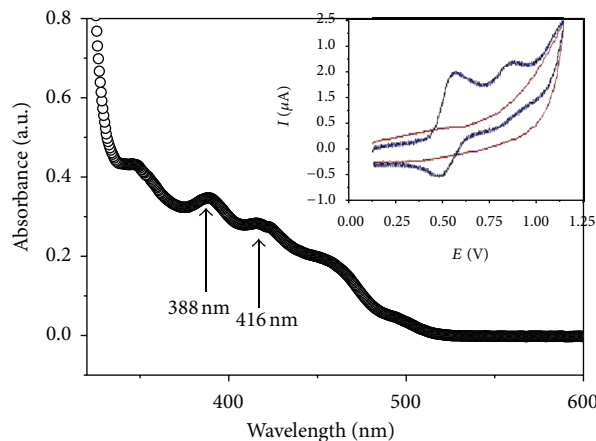


FIGURE 1: Absorption spectra of (tpbi)₂Ir(acac) material. The inset was cyclic voltammetry curve of the iridium dye.

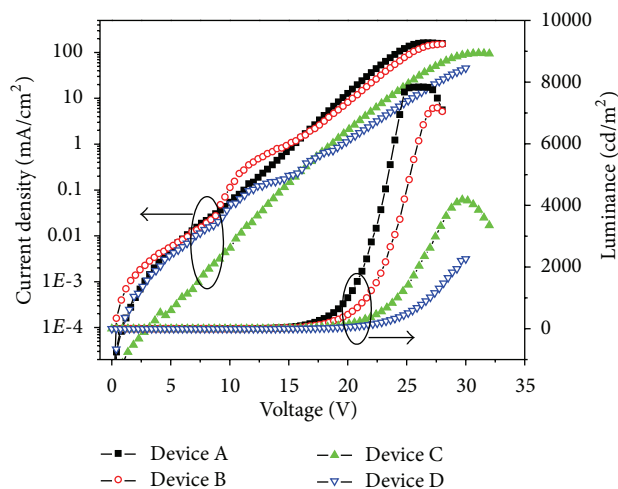


FIGURE 2: Current density-voltage-luminance characteristics of four doping concentration devices.

3. Results and Discussions

In order to identify the energy transferring from blended polymer host to the doped (tpbi)₂Ir(acac), the absorption spectra and cyclic voltammetry curve of iridium dye were displayed in Figure 1. There were two absorptive peaks at 388 nm and 416 nm, which were covered by the photoluminescence spectra of mixed PBD:PFO, which indicated the feasibility of energy transfer from host to doped dye. From the absorption and cyclic voltammetry curve, the highest occupied molecular orbital (HOMO) and lowest unoccupied molecular orbital (LUMO) energy level were 5.1 eV and 2.7 eV, respectively. The current density-voltage-luminance characteristics of four doping concentration devices were shown in Figure 2. The turn-on voltage (defined as the voltage when organic device luminance reached 1 cd/m²) of 1%, 2%, 4%, and 8% doping concentration devices were 10.0 V, 9.8 V, 12.4 V, and 12.2 V, respectively. The lower doped devices (1% and 2%) showed higher current density than the heavy doped devices (4% and 8%) at the same driving bias. The shift of current density-voltage curves to higher voltages as doping concentration

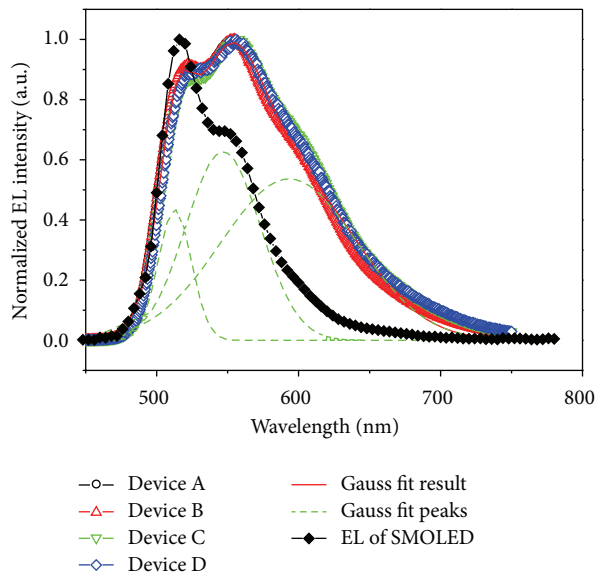


FIGURE 3: The normalized EL spectra of devices A, B, C, and D at 20 V and Gauss fit results. EL spectrum of SMOLED was shown for comparing.

increasing could be attributed to charge-trapping effect [19]. When more iridium complex was doped in host material, more trapping center formed for the free carriers because the HOMO and LUMO level of $(\text{tpbi})_2\text{Ir}(\text{acac})$ were between that of PFO and PBD blended host, so that the current density of device became lower at the same driving voltage when increasing the doping concentration. As the forward bias increased (over turn-on voltage), the luminance of organic devices enhanced sharply and reached to the maximum values of 7841 cd/cm^2 (at 25.6 V), 7171 cd/cm^2 (at 27.2 V), 4180 cd/cm^2 (at 29.6 V), and 2264 cd/cm^2 (at 30 V) for devices A, B, C, and D, respectively. The device luminance changing trends of different doping concentration devices were in conformity with the current density, which was that higher doping concentration organic device showed lower device luminance at the same bias. The more the doped phosphor dye in the polymer layer, the more the traps or lacunas formed in the organic device, which would capture more charge carriers and affect the emission process of device.

The normalized EL spectra of polymer devices A, B, C, and D at 20 V bias were suggested in Figure 3. There were two obvious emission peaks around 522 nm and 554 nm, which were attributed to the emission of $(\text{tpbi})_2\text{Ir}(\text{acac})$. The emission peak coming from phosphor dye could be identified by small molecular organic light-emitting diodes (SMOLED) with CBP as host material. The SMOLED doped by the phosphor dye had been fabricated with device structure ITO/CuPc (40 nm)/ α -NPD (45 nm)/CBP: $(\text{tpbi})_2\text{Ir}(\text{acac})$ (3 wt%, 30 nm)/BCP (20 nm)/Alq₃ (20 nm)/LiF (1 nm)/Al (100 nm), and EL spectrum of the device was also shown in Figure 3 for comparing [18]. But the strongest emission peak was changed from 522 nm to 554 nm for polymer device, and the spectrum width of PLED was nearly double that of SMOLED. The spectrum of polymer light-emitting diodes covered from

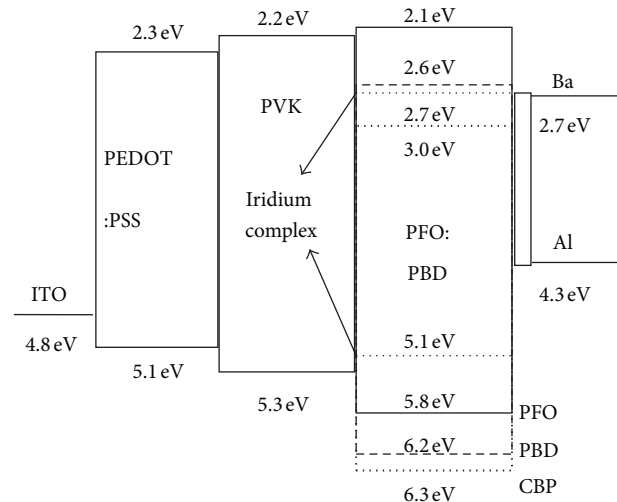


FIGURE 4: Energy level diagram of polymer light emitting device fabricated in this study.

490 nm to 690 nm, and full width at half-maximum (FWHM) of emission spectrum was 116 nm (from 504 nm to 620 nm), which was 68 nm for SMOLED (from 500 nm to 568 nm). There was an obvious spectra extension at the long wave region ($\sim 600 \text{ nm}$), which might be caused by the blended polymer host materials. To describe the phenomenon clearly, energy level of polymer device was shown in Figure 4. In small molecular organic device with $(\text{tpbi})_2\text{Ir}(\text{acac})$ doped in CBP host, the HOMO and LUMO energy level of iridium complex and CBP were 5.1 eV and 2.7 eV, 6.3 eV, and 3.0 eV, respectively. $(\text{tpbi})_2\text{Ir}(\text{acac})$ molecules could be excited by those excitons with energy transfer from CBP host, but the kinds of excitons formed in CBP were simple because of single energy level structure. In the blended polymer host structure of this research, the HOMO and LUMO energy level of PFO and PBD were 5.8 eV and 2.1 eV, 6.2 eV, and 2.6 eV, respectively. The HOMO and LUMO energy level of $(\text{tpbi})_2\text{Ir}(\text{acac})$ could be identified by the cyclic voltammetry curve as shown in the inset of Figure 1. After doping iridium complex in the blended polymer host, the phosphor dye could be excited by trapping the free carriers directly in the host layer and accepting energy transfer from host excitons. The blended polymer host promoted the energy transferring from different energy level to phosphorescent dye, which could extend the emission spectrum to yellow light region width of polymer emission device. The Gaussian multipeak simulation indicated that there were three peaks (513 nm, 548 nm, and 596 nm) in the phosphor emission spectrum, and the total fitting spectrum curve was highly consistent with the test result as shown in Figure 3. The emission peak at 596 nm occupied near 50% of the total emission spectra area, which indicated this energy level accepted about 50% energy transfer from polymer host and formed effective light emission.

PEDOT:PSS layer spun on ITO films was used to improve the substrate smoothness, and the other important role was that this film has approximate work function with ITO anode [20], which would be good for hole injection due to the

TABLE 1: Some detailed characteristics of four organic devices with different doping concentrations, including turn-on voltage, maximum luminance, current density at 20 V, maximum current, and power efficiency.

Device	V_{on} (V)	L_{max} (cd/m ²)	$J_{20\text{V}}$ (mA/cm ²)	$\eta_{p\text{max}}$ (lm/W)	$\eta_{l\text{max}}$ (cd/A)
Device A	10.0	7841	12.8	1.84	9.95
Device B	9.8	7171	8.2	1.54	6.96
Device C	12.4	4180	2.1	1.44	7.52
Device D	12.2	2264	1.2	0.80	5.78

lower height of injection barrier. PVK was a very good hole transporting and wide band gap material but not an electron transporting material [21], so that PVK could be used as hole transporting layer with blocking electronic function. PVK was also a high molecular weight material, which was helpful in forming thin dense films with high uniformity and improving the film-forming quality for the emitting layer and finally improving the stability of device. The HOMO and LUMO level of PFO were estimated to be 5.8 eV and 2.1 eV [22], so that the wide band gap (3.7 eV) of PFO made it difficult to form ohm contacts for free carriers injecting into emission layer, which was unsuitable to obtain high efficiency device. In order to decrease the LUMO energy level barrier and promote electron transporting ability, 30 wt% PBD was mixed to form blended host matrix. PBD was widely used as electron transporting layer, which showed the HOMO and LUMO level of 6.2 eV and 2.6 eV, respectively [23]. The LUMO level of PBD was very near to the work function of Ba layer, which was inserted between PFO:PBD blended layer and Al cathode with a super-thin film thickness. The 4 nm Ba film promoted the injection of electrons from cathode to host layer to be much easier than that directly from Al metal (work function, 4.7 eV). The addition of PVK transporting layer, PFO:PBD blended host layer, and Ba buffer layer was propitious to increase the stability and efficiency of polymer device.

The power efficiency (η_p) and current efficiency (η_l) of four doping concentration devices (device A: 1 wt%, device B: 2 wt%, device C: 4 wt%, and device D: 8 wt%) at different biases were shown in the Figure 5. Both η_p and η_l initially increased to the maximum value and then decreased as the bias voltage increased for those polymer devices. The maximum η_l of device A, B, C, and D were 9.95 cd/A (at 17.2 V), 6.96 cd/A (at 20.8 V), 7.52 cd/A (at 21.4 V), and 5.78 cd/A (at 26.2 V), respectively. The maximum luminance and power efficiency of four devices (shown in Table 1) became lower when increasing the doping concentration. The doping phosphor dye was not only the emission center but also traps for free carriers in emission layer, which could be predicted from the device energy level diagram shown in Figure 4. More free carriers would be trapped in the devices when adding more phosphor dye in the blended host layer, which would affect the current density, numbers of emission elements, and finally the whole device efficiency. This point could be proved by the current density curve of four devices at high driving voltages shown in Figure 2. The current density of device A (1 wt% doping concentration) was 12.8 mA/cm² and decreased to 1.2 mA/cm² for device D (8 wt% doping concentration) at 20 V forward bias, which were listed in Table 1. The

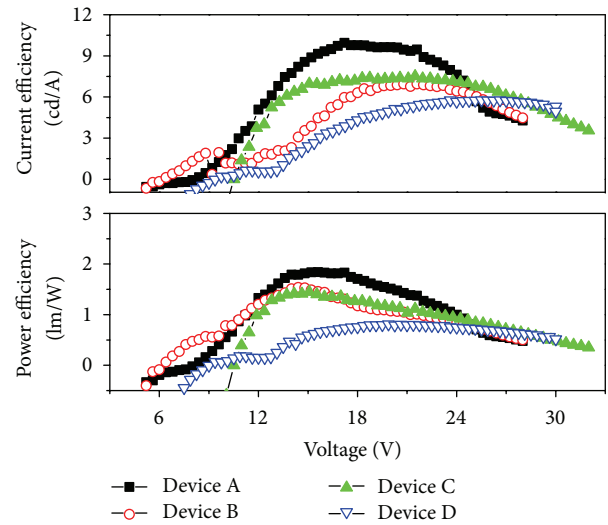


FIGURE 5: The power efficiency and current efficiency of four doping devices at different biases.

roll-off of external quantum efficiency of electroluminescent device at large current density was due to triplet-triplet (T-T) annihilation for most phosphorescent organic device. Endo et al. analyzed T-T annihilation for Ir(ppy)₃ doped CBP host devices, and a best fit of the model to the data was obtained [24]. Almost all organic devices indicated a gradual decrease in efficiency at the high current density (according to high voltage). The quantum efficiency of light emission (η) can be calculated from the following equation:

$$\frac{\eta}{\eta_0} = \frac{J_0}{4J} \left(\sqrt{\frac{1+8J}{J_0}} - 1 \right). \quad (1)$$

In (1), η_0 is the quantum efficiency without triplet-triplet annihilation, and J_0 in (2) is the "onset" current density at $\eta = \eta_0/2$:

$$J_0 = \frac{4qd}{k_{\text{TT}}\tau^2}. \quad (2)$$

In which q is the electron charge, d is the thickness of the exciton formation zone, τ is the phosphorescent life time, and k_{TT} is the T-T annihilation rate constant. As the current density (driving bias) increased, the efficiency annihilation became more obvious as shown in (1). For comparing, the turn-on voltage (V_{on}), maximum lumiance (L_{max}), current density at 20 V ($J_{20\text{V}}$), maximum power efficiency ($\eta_{p\text{max}}$),

and current efficiency ($\eta_{l\max}$) were list in Table 1. Stable green light emission, wide emission spectra, and high efficiency of 9.95 cd/A could be achieved with the 1 wt% doping concentration polymer device with blended host materials.

4. Conclusions

Different doping concentration polymer organic devices with iridium complex doped in PFO:PBD blended host material were fabricated using spun coat process. The EL spectra of devices indicated stable green light emission from (tpbi)₂Ir(acac) with two main peaks at 522 nm and 554 nm and a wide FWHM of 116 nm from 504 nm to 620 nm. Maximum current efficiency of 9.95 cd/A could be reached at 17.2 V bias and slowly rolled off as the driving voltage increased. High quality, easy fabricated white light emission polymer device could be anticipated with this wide emission spectra device structure.

Conflict of Interests

The authors declare that there is no conflict of interests regarding the publication of this paper.

Acknowledgments

This work is partially supported by the National Science Foundation of China (NSFC) via Grant no. 61006036 and “the Fundamental Research Funds for the Central Universities” (ZYGX2011X012). One of the authors (J. Wang) thanks the Program for New Century Excellent Talents in University (NCET-10-0299).

References

- [1] K. Goushi, K. Yoshida, K. Sato, and C. Adachi, “Organic light-emitting diodes employing efficient reverse intersystem crossing for triplet-to-singlet state conversion,” *Nature Photonics*, vol. 6, no. 4, pp. 253–258, 2012.
- [2] J. Y. Lee, “Charge trapping effect in phosphorescent organic light-emitting diodes,” *Molecular Crystals and Liquid Crystals*, vol. 498, pp. 131–139, 2009.
- [3] C. W. Tang and S. A. VanSlyke, “Organic electroluminescent diodes,” *Applied Physics Letters*, vol. 51, p. 913, 1987.
- [4] J. Lee, C. Huang, C. Hsiao, M. Leung, C. Yang, and C. Chao, “Blue phosphorescent organic light-emitting device with double emitting layer,” *Applied Physics Letters*, vol. 94, Article ID 223301, 2009.
- [5] S. Reineke, F. Lindner, G. Schwartz et al., “White organic light-emitting diodes with fluorescent tube efficiency,” *Nature*, vol. 459, no. 7244, pp. 234–238, 2009.
- [6] F. So and D. Kondakov, “Degradation mechanisms in small-molecule and polymer organic light-emitting diodes,” *Advanced Materials*, vol. 22, no. 34, pp. 3762–3777, 2010.
- [7] M. Wu, Z. Gong, A. J. C. Kuehne et al., “Hybrid GaN/organic microstructured light-emitting devices via ink-jet printing,” *Optics Express*, vol. 17, no. 19, pp. 16436–16443, 2009.
- [8] J. H. Burroughes, D. D. C. Bradley, A. R. Brown et al., “Light-emitting diodes based on conjugated polymers,” *Nature*, vol. 347, pp. 539–541, 1990.
- [9] T. R. Hebner, C. C. Wu, D. Marcy, M. H. Lu, and J. C. Sturm, “Ink-jet printing of doped polymers for organic light emitting devices,” *Applied Physics Letters*, vol. 72, no. 5, pp. 519–521, 1998.
- [10] C. D. Müller, A. Falcou, N. Reckefuss et al., “Multi-colour organic light-emitting displays by solution processing,” *Nature*, vol. 421, no. 6925, pp. 829–833, 2003.
- [11] M. C. Gather, A. Köhnen, A. Falcou, H. Becker, and K. Meerholz, “Solution-processed full-color polymer organic light-emitting diode displays fabricated by direct photolithography,” *Advanced Functional Materials*, vol. 17, no. 2, pp. 191–200, 2007.
- [12] D. Kabra, L. P. Lu, M. H. Song, H. J. Snaith, and R. H. Friend, “Efficient single-layer polymer light-emitting diodes,” *Advanced Materials*, vol. 22, no. 29, pp. 3194–3198, 2010.
- [13] K. S. Yook, S. E. Jang, and J. Y. Lee, “Efficiency improvement of solution processed blue phosphorescent devices using high triplet energy electron transport layer,” *Electrochemical and Solid-State Letters*, vol. 13, no. 10, pp. J122–J124, 2010.
- [14] L.-C. Ko, T.-Y. Liu, C.-Y. Chen et al., “Multi-layer organic light-emitting diodes processed from solution using phosphorescent dendrimers in a polymer host,” *Organic Electronics*, vol. 11, no. 6, pp. 1005–1009, 2010.
- [15] H. B. Wu, G. J. Zhou, J. H. Zou et al., “Efficient polymer white-light-emitting devices for solid-state lighting,” *Advanced Materials*, vol. 21, no. 41, pp. 4181–4184, 2009.
- [16] Q. L. Niu, Y. Zhang, Y. L. Wang, X. Wang, and M. He, “High-efficiency conjugated-polymer-hosted blue phosphorescent light-emitting diodes,” *Chinese Science Bulletin*, vol. 57, pp. 3639–3643, 2012.
- [17] Q. Niu, X. Wang, J. Zhou, Y. Wang, and Y. Zhang, “Effect of methanol treatment on performance of phosphorescent dye doped polymer light-emitting diodes,” *Synthetic Metals*, vol. 160, no. 21–22, pp. 2381–2384, 2010.
- [18] J. Wang, X.-Q. Wei, H.-B. Rao, J.-B. Cheng, and Y.-D. Jiang, “High-efficiency and high-stability phosphorescent OLED based on new Ir complex,” *Acta Physica Sinica*, vol. 56, no. 2, pp. 1156–1161, 2007.
- [19] H. Liu, P. Wang, J. He et al., “High-efficiency endothermic energy transfer in polymeric light-emitting devices based on cyclometalated Ir complexes,” *Applied Physics Letters*, vol. 92, Article ID 023301, 2008.
- [20] L. Müller-Meskamp, Y. H. Kim, T. Roch et al., “Efficiency enhancement of organic solar cells by fabricating periodic surface textures using direct laser interference patterning,” *Advanced Materials*, vol. 24, no. 7, pp. 906–910, 2012.
- [21] M. S. Soh, S. A. G. Santamaria, E. L. Williams, M. Pérez-Morales, H. J. Bolink, and A. Sellinger, “Solution processable high band gap hosts based on carbazole functionalized cyclic phosphazene cores for application in organic light-emitting diodes,” *Journal of Polymer Science B*, vol. 49, no. 7, pp. 531–539, 2011.
- [22] X. Wu, Y. Liu, Y. Wang et al., “Highly efficient near-infrared emission from binuclear cyclo-metallated platinum complexes bridged with 5-(4-octyloxyphenyl)-1,3,4-oxadiazole-2-thiol in PLEDs,” *Organic Electronics*, vol. 13, no. 5, pp. 932–937, 2012.
- [23] Y. Mizuno, I. Takasu, S. Uchikoga et al., “Fluorinated carbazole derivatives as wide-energy-gap host material for blue phosphorescent organic light-emitting diodes,” *The Journal of Physical Chemistry C*, vol. 116, no. 39, pp. 20681–20687, 2012.
- [24] A. Endo, K. Sato, K. Yoshimura et al., “Efficient up-conversion of triplet excitons into a singlet state and its application for organic light emitting diodes,” *Applied Physics Letters*, vol. 98, no. 8, Article ID 083302, 2011.

Research Article

Optical Limiting Using the Two-Photon Absorption Electrical Modulation Effect in HgCdTe Photodiode

Haoyang Cui, Junjie Yang, Jundong Zeng, and Zhong Tang

School of Electronic and Information Engineering, Shanghai University of Electric Power, 2103 Pingliang Road, Shanghai 200090, China

Correspondence should be addressed to Haoyang Cui; cuihy@shiep.edu.cn

Received 16 August 2013; Accepted 5 September 2013

Academic Editors: W. Hu, S. Jit, and F. Yue

Copyright © 2013 Haoyang Cui et al. This is an open access article distributed under the Creative Commons Attribution License, which permits unrestricted use, distribution, and reproduction in any medium, provided the original work is properly cited.

The electrical modulation properties of the output intensity of two-photon absorption (TPA) pumping were analyzed in this paper. The frequency dispersion dependence of TPA and the electric field dependence of TPA were calculated using Wherrett theory model and Garcia theory model, respectively. Both predicted a dramatic variation of TPA coefficient which was attributed into the increasing of the transition rate. The output intensity of the laser pulse propagation in the pn junction device was calculated by using function-transfer method. It shows that the output intensity increases nonlinearly with increasing intensity of incident light and eventually reaches saturation. The output saturation intensity depends on the electric field strength; the greater the electric field, the smaller the output intensity. Consequently, the clamped saturation intensity can be controlled by the electric field. The prior advantage of electrical modulation is that the TPA can be varied extremely continuously, thus adjusting the output intensity in a wide range. This large change provides a manipulate method to control steady output intensity of TPA by adjusting electric field.

1. Introduction

Two-photon absorption (TPA) is a third-order nonlinear absorption process which is closely related to the imaginary part of nonlinear susceptibility of the material [1]. Because TPA has different selection rules than one-photon absorption (OPA), it is widely used in the spectroscopy analyzing of semiconductor [2]. Moreover, two-photon absorption (TPA) is an effective process to fulfill the nonlinear optical devices [3] owing to its high transparency at low incident intensity while blocking the transmission at high intensities. Although some theoretical investigations [4, 5] and experimental measurements [6] about TPA properties have been reported early, the constant electric field effects of TPA on the transmission intensity have not received much attention. This is surprising considering that strong fields are often present in semiconductor-based photonic devices, such as pn junction photovoltaic device. The lack of research is detrimental to the application of nonlinear optical devices.

In this paper, the dispersion dependence of TPA on photon frequency is calculated using second-order perturbation theory. Then, the electric field modulation effect of two-photon absorption coefficient (TPAC) in HgCdTe photodiode is

simulated from a two-band model. The results show that the TPAC in space charge region (SCR) is enhanced dramatically by the build-in electric field. A TPA Franz-Keldysh Effect (FKE) mentioned by Garcia is adapted to interpret this phenomenon. On this basis, the dependence of output intensity on electric field is calculated using the TPA modulation relationship. It shows that the output intensity can be manipulated continuously by adjusting the bias voltage.

2. Theory Model

2.1. Frequency Dispersion Dependence of TPAC. The two-photon process where the two-photon transition occurs from an initial state $|i\rangle$ to a final state $|f\rangle$ involving simultaneous absorption of two photons was theoretically predicted by Göppert-Mayer [7] in 1931. Since the transition probability is proportional to $\delta(E_f - E_i - \hbar\omega_1 - \hbar\omega_2)$, it may be obtained from Fermi golden rule:

$$W^{(2)} = \frac{2\pi}{\hbar} \sum |M_{cv}^{(2)}|^2 \delta(E_c(\vec{k}_c) - E_v(\vec{k}_v) - 2\hbar\omega), \quad (1)$$

where \vec{k} is the wave vector of the internal motion of the exciting and $M_{cv}^{(2)}$ is the transition matrix element, respectively. In order to solve (1), the energy band, momentum matrix element, and the intermediate state should be approximated to simplify the calculation. However, the approximations and simplifying assumptions used in this process would result in a large discrepancy between the calculation and experiment results of TPAC. In the computing models presented in the literatures, Wherrett [8] model has been generally recognized. From the second-order perturbation theory, the interaction matrix element H'_{fi} between initial state $|i\rangle$ and final state $|f\rangle$ associated with the absorption of one photon can be obtained as:

$$M_{cv}^{(2)} = \frac{\sum_i H'_{ci} H'_{iv}}{E_{iv}(\vec{k}) - \hbar\omega}, \quad (2)$$

$$H'_{fi} = \frac{q}{im\omega} \left(\frac{2\pi I}{nc} \right)^{1/2} \varepsilon \cdot p_{fi},$$

where n , p_{fi} , and ε are refractive index, momentum matrix element, and radiation polarization, respectively. For the spin degeneracy for the bands, the TPA transition rate $W^{(2)}$ can be written as

$$W^{(2)} = \frac{1}{\pi\hbar} \left[\left(\frac{2m_{cv}}{\hbar^2} \right)^{3/2} (2\hbar\omega - E_c - E_v)^{1/2} \right] \times \left[\left(\frac{q}{m\omega} \right)^4 \left(\frac{2\pi I}{nc} \right)^2 \times \left\langle \left| S_{cv}^{(2)} \left(\frac{(2m_{cv})^{1/2} (2\hbar\omega - E_c - E_v)^{1/2}}{\hbar} \right) \right|^2 \right\rangle \right], \quad (3)$$

where $S_{cv}^{(2)} = \sum_i p_{ci} p_{iv} [E_{iv} ((2m_{cv})^{1/2} (2\hbar\omega - E_c - E_v)^{1/2} / \hbar) - \hbar\omega]^{-1}$ and p represents $\varepsilon \cdot p$. Retaining the matrix element corresponding to the direct contribution, TPAC can be expressed as

$$\beta(\omega) = 2^9 \sqrt{2\pi} \left(\frac{q^2}{\hbar c} \right)^2 \frac{f_2}{f} \frac{\hbar P}{n_2 E_g^3} \frac{(2\hbar\omega/E_g - 1)^{3/2}}{(2\hbar\omega/E_g)^5} \quad (4)$$

$$= A \frac{(2\hbar\omega/E_g - 1)^{3/2}}{(2\hbar\omega/E_g)^5},$$

where c , q , E_g and $\hbar\omega$ are speed of sound, electron charge, energy gap, and incident photon energy, respectively. $P \propto p_{cv} \hbar/m$ is Kane momentum parameters. f is defined as the numerical factor. Equation (4) shows the frequency dispersion relation of TPAC.

Figure 1 shows the frequency dispersion relation of TPA. It can be seen that the TPAC is almost equal to zero for an incident photon energy less than half energy gap; this shows that no transition occurs between energy bands. The TPAC will continuously increase with the photon energy when the photon energy is larger than half energy gap. Then, the TPAC will

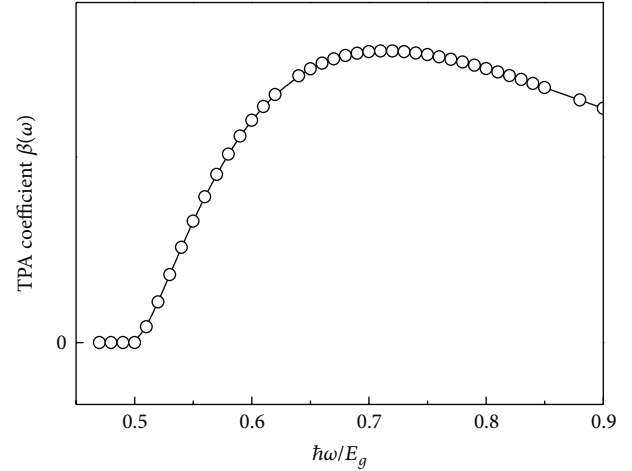


FIGURE 1: The calculating frequency dependence of TPAC and incident photon energy.

show a decreasing tendency if the photon energy increased more. This indicates that there is a maximum value in the TPAC. The effects of the external electric field on TPAC have been more complicated; in the electric field, the problem is further complicated and will be discussed below.

2.2. Electric Field Dependence of TPAC. A two-band model consisting of heavy-hole and light-hole bands mentioned by Garcia [4] is used to discuss the dependence of TPAC on electric field here. Using a nonparabolic approximation of the state's density, the impact of electric field intensity on the TPA transition probabilities can be derived from the Fermi golden rule [4]:

$$W_2 = \frac{1}{(2\pi)^2} \sum_n \sum_{n'} \int dk W^{(2)}(k),$$

$$W^{(2)}(k) = \frac{|P_{vc}|^2}{2\pi\hbar} \left(\frac{2\pi m_c \omega N}{mk \cdot \hat{z}} \right)^2 \left(\frac{\hbar^2}{2MFe} \right)^{2/3} \times \left| I_N \left(\frac{ek \cdot \hat{z} A_0}{m_c \omega c} \right) \right|^2 [Ai(\delta_2) a_n^c a_n^v]^2 \times \delta(E_{k\perp}^c + E_{k'\perp}^v + E_e - E_h + E_g - 2\hbar\omega), \quad (5)$$

where P_{vc} , F , $Ai(z)$, m_c , m_v , and m_u are interband momentum matrix element, electric field, Airy function, effective mass of electron and hole, and the reduced mass, respectively. In the whole excitation process, principle of energy conservation is satisfied by δ function, while momentum conservation is satisfied by $\Delta k = k_c - k_v = 0$; thus the TPAC can be derived as

$$\beta^{(2)}(\omega, F) = \left(\frac{5\pi}{2\sqrt{3}} \right) \frac{K(E_p E_g E_\mu)^{1/2}}{n^2 (2\hbar\omega)^5} \times \left\{ 2 \left[\varepsilon_0^2 Ai^2(\zeta_0) - \zeta_0 |Ai'(\zeta_0)|^2 \right] - Ai(\zeta_0) Ai'(\zeta_0) \right\}, \quad (6)$$

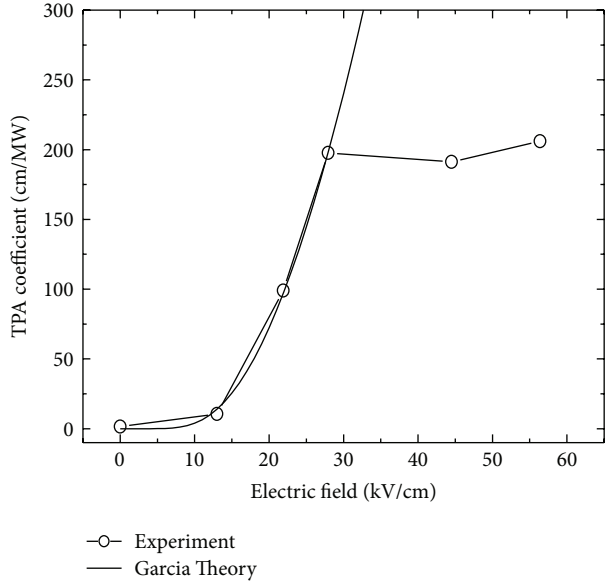


FIGURE 2: The dependence of TPAC on the build-in electric field strength. The circle points are the experimental data, and the line represents the calculation data.

where $\epsilon_0 = (2\hbar\omega - E_g)/E_\mu$, $E_\mu = (\hbar^2 e^2 F^2 / 2m_\mu)^{1/3}$, is the characteristic energy of the dc electric field. Because of the introduction of this parameter, the TPAC will change with the electric field strength. E_p is the transition matrix. $K = 1940 \text{ cm/GW (eV)}$ is a material-independent constant.

Using the expression in (6), the TPAC at different electric field is simulated (shown in Figure 2). We compared the simulation results with the two-photon absorption experimental results of HgCdTe photodiode [6]. The HgCdTe photodiode used in this work was prepared by the literature methods [6, 9–12]. As one can see, the calculated and the experimental data have a similar dependence on the electric field at $0 < F < 30 \text{ kV/cm}$. However, if the electric field $F > 30 \text{ kV/cm}$, the calculation data still increase, while the experimental TPAC shows saturation. This can be attributed to the saturation of the electric field in the pn junction in this range, and the electric field strength in the SCR will not increase anymore.

Figure 2 shows that the TPAC at 0 V ($\beta_1 = 10.5 \text{ cm/MW}$) has been enhanced by about seven times comparing to zero electric field ($\beta_0 = 1.5 \text{ cm/MW}$). When the built-in electric field varies from 13.4 kV/cm to 30 kV/cm, TPAC will be enhanced into 198 cm/MW, about 19 times increasing. This significant enhancement is attributed to the FEK of the TPAC in SCR. The absorption coefficient increased in the strong electric field of SCR by increasing the coupling intensity of electron and hole wave functions. FKE occurs because the electric field assisted tunneling process in SCR makes the effective energy gap shrink for an electron in the interband transition. The band gap shrinkage is proportional to the electric field [13] as $\Delta E_g \sim F$. Consequently, the electrons exited from valance band have more probability to transmit into the conduction band. This mechanism has made the TPAC within the SCR increase [6, 14].

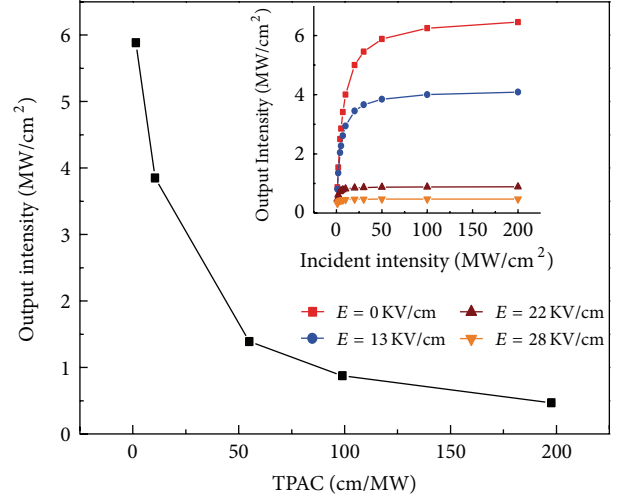


FIGURE 3: The dependence of output intensity on TPAC when the incident intensity is 50 MW/cm^2 . The insert is the dependence of output intensity on incident intensity at different electric field.

2.3. *Electric Field Dependence of Output Intensity.* Based on the analysis given above, it can be known that the TPAC can be adjusted effectively by varying the electric field applied, thus changing the output light intensity. Undoubtedly, this TPAC manipulating effect is very attractive for the nonlinear optical devices such as optical limiter. In the following, we will simulate the effects of TPAC manipulation on the output intensity. The output intensity of pn junction can be solved using function-transfer method [15]:

$$I_{n+1} \approx I_n - \frac{\beta I_n^2 \Delta x}{(1 + \beta I_n \Delta x)}, \quad (7)$$

where Δx is the cell thickness of absorption layer and I_n is the incident intensity of n layer. As a result of back-illuminated, the incident light passes through the flat band of p region first and then into the SCR. Comparing with the thick base region, the thickness of the heavy doped emitter can be neglected. Therefore, only the optical loss in flat belt layer and SCR is considered here. Using the conclusion of TPAC modulation mentioned above, the effects of TPAC manipulation on the output intensity can be simulated, which is shown in Figure 3.

It can be seen from Figure 3 that, with the TPAC increasing, the output intensity will decrease dramatically. This can be attributed the enhancement of TPA in SCR, resulting in more carriers that are excited by the photons, and the output intensity transmitted from material is weakened continually. The inset of Figure 3 shows that the output intensity increases non-linearly with increasing intensity of incident light and eventually reaches saturation. The output saturation intensity depends on the electric field strength the greater the electric field, the smaller the output intensity. This shows that the clamped saturation intensity can be controlled by the electric field.

3. Conclusion

In conclusion, we calculated the dependence of electric field on the TPAC and the output intensity in pn junction photodiode. Because of the TPA FKE, the TPAC could be manipulated by adjusting the electric field within the SCR. We simulated the dependence of electric field strength on the output intensity. It shows that the clamped saturation intensity can be controlled by the electric field. From the analysis of nonlinear TPA in the semiconductor, one can obtain a method to control steady output intensity of TPA pumping by adjusting electric field or bias voltage. Since the TPA is an important mechanism in semiconductors, our initial result on the electric field induced tunability of TPA, and its influence on the output intensity would can be very useful for the nonlinear optical device.

Conflict of Interests

The authors declared that they have no conflict of interests to this work.

Acknowledgments

This project was supported by the National Natural Science Foundation of China (61107081, 61202369) and Innovation Program of Shanghai Municipal Education Commission of China (12ZZ176).

References

- [1] J. Jiang, Y. Fu, N. Li et al., "Two-photon-absorption-induced nonlinear photoresponse in GaAs/AlGaAs quantum-well infrared photodetectors," *Applied Physics Letters*, vol. 85, article 3614, no. 16, 3 pages, 2004.
- [2] F. R. Ahmad, Y. W. Tseng, M. A. Kats, and F. Rana, "Energy limits imposed by two-photon absorption for pulse amplification in high-power semiconductor optical amplifiers," *Optics Letters*, vol. 33, p. 1041, 2008.
- [3] S. Krishnamurthy, Z. G. Yu, S. Guha, and L. Gonzalez, "High intensity light propagation in InAs," *Applied Physics Letters*, vol. 89, no. 16, article 161108, 3 pages, 2006.
- [4] H. Garcia, "Tunneling assisted two-photon absorption: the nonlinear Franz-Keldysh effect," *Physical Review B*, vol. 74, no. 3, Article ID 035212, 6 pages, 2006.
- [5] J. K. Wahlstrand, S. T. Cundiff, and J. E. Sipe, "Polarization dependence of the two-photon Franz-Keldysh effect," *Physical Review B*, vol. 83, no. 23, Article ID 233201, 2011.
- [6] H. Y. Cui, Z. F. Li, Z. L. Liu et al., "Modulation of the two-photon absorption by electric fields in HgCdTe photodiode," *Applied Physics Letters*, vol. 92, no. 2, Article ID 021128, 3 pages, 2008.
- [7] M. Göppert-Mayer, "Über Elementarakte mit zwei Quantensprüngen," *Annalen der Physik*, vol. 401, no. 3, pp. 273–295, 1931.
- [8] B. S. Wherrett, "Scaling rules for multiphoton interband absorption in semiconductors," *Journal of the Optical Society of America B*, vol. 1, no. 1, pp. 67–72, 1984.
- [9] W. D. Hu, X. S. Chen, F. Yin et al., "Analysis of temperature dependence of dark current mechanisms for long-wavelength HgCdTe photovoltaic infrared detectors," *Journal of Applied Physics*, vol. 105, no. 10, Article ID 104502, 2009.
- [10] W. D. Hu, X. S. Chen, Z. H. Ye et al., "Polarity inversion and coupling of laser beam induced current in as-doped long-wavelength HgCdTe infrared detector pixel arrays: experiment and simulation," *Applied Physics Letters*, vol. 101, Article ID 181108, 10 pages, 2012.
- [11] F. Yin, W. D. Hu, B. Zhang et al., "Simulation of laser beam induced current for HgCdTe photodiodes with leakage current," *Optical and Quantum Electronics*, vol. 41, no. 11-13, pp. 805–810, 2009.
- [12] W. D. Hu, X. S. Chen, Z. H. Ye et al., "Dependence of ion-implant-induced LBIC novel characteristic on excitation intensity for Long-wavelength HgCdTe-based photovoltaic infrared detector pixel arrays," *IEEE Journal of Selected Topics in Quantum Electronics*, vol. 19, Article ID 4100107, 2013.
- [13] S. Jongthammanurak, J. Liu, K. Wada et al., "Large electro-optic effect in tensile strained Ge-on-Si films," *Applied Physics Letters*, vol. 89, no. 16, Article ID 161115, 2006.
- [14] S. Krishnamurthy, K. Nashold, and A. Sher, "Two-photon absorption in GaN, GaInN, and GaAlN alloys," *Applied Physics Letters*, vol. 77, no. 3, pp. 355–357, 2000.
- [15] J. Jiang, N. Li, G.-B. Chen et al., "Free-electron laser induced nonlinear optical absorption in semiconductors," *Acta Physica Sinica*, vol. 52, no. 6, p. 1403, 2003.

Research Article

The Effect of Metal-Semiconductor Contact on the Transient Photovoltaic Characteristic of HgCdTe PV Detector

Haoyang Cui, Yongpeng Xu, Junjie Yang, Naiyun Tang, and Zhong Tang

School of Electronic and Information Engineering, Shanghai University of Electric Power, 2103 Pingliang Road, Shanghai 200090, China

Correspondence should be addressed to Haoyang Cui; cuihy@shiep.edu.cn

Received 14 August 2013; Accepted 1 September 2013

Academic Editors: W. Hu, S. Jit, and F. Yue

Copyright © 2013 Haoyang Cui et al. This is an open access article distributed under the Creative Commons Attribution License, which permits unrestricted use, distribution, and reproduction in any medium, provided the original work is properly cited.

The transient photovoltaic (PV) characteristic of HgCdTe PV array is studied using an ultrafast laser. The photoresponse shows an apparent negative valley first, then it evolves into a positive peak. By employing a combined theoretical model of pn junction and Schottky potential, this photo-response polarity changing curves can be interpreted well. An obvious decreasing of ratio of negative valley to positive peak can be realized by limiting the illumination area of the array electrode. This shows that the photoelectric effect of Schottky barrier at metal-semiconductor (M/S) interface is suppressed, which will verify the correctness of the model. The characteristic parameters of transient photo-response induced from p - n junction and Schottky potential are extracted by fitting the response curve utilizing this model. It shows that the negative PV response induced by the Schottky barrier decreases the positive photovoltage generated by the pn junction.

1. Introduction

Compared with Quantum-Well-Infrared Photodetector (QWIP), HgCdTe Focal-Plane Array (FPAs) have the advantages of high detection rate, high response speed, and wide detection band and have been widely applied in aerospace infrared optical remote sensors, scientific satellites, military defense and meteorological observation [1–3]. To realize the conversion of optical signals into electrical signals, the photo carriers will be injected into the readout circuit through the HgCdTe-Metal interface in the basic pixel structure. This requires the electrode forming an Ohmic contact at the M/S interface [4]. Generally, the interface barrier layer will become very thin if the metal contact with the heavily doped n^+ -HgCdTe, so that the carriers can tunnel through these barriers. Thus, M/S interface can form an Ohmic contact. But due to the fragile nature of the HgCdTe material, p HgCdTe is not easy to form Ohmic contacts with metal, and it is even possible to form a Schottky contact [5, 6]. Thus the I - V characteristics will be impacted by the rectified characteristic of the M/S interface electric field. The more obviously the Schottky junction effect is, the serious influence of I - V characteristic is likely to be suffered. Currently, this approach has become a common means to research interface contact

characteristics and evaluate the quality of Ohmic electrodes [7–9]. Nevertheless, there are still some deficiencies using this method. Firstly, the interface information can only be extracted from the I - V characteristic when the Schottky junction effects become more serious. Secondly, the impact of Schottky junction effect on the PV conversion mechanism cannot be determined from I - V characteristic measurements.

The transient photovoltage (TPA) measurement will lead to a variety of novel physical phenomena and a diversity of new phases which the conventional optical characterization methods are difficult to observe, and this will have a special advantage for the enrichment and development of semiconductor optical theory. With the ultrafast pulsed laser excitation, optical devices will generate a lot of photo-generated carriers, which is very sensitive to the internal electric field of the semiconductor; thus, the transient photovoltaic properties demonstrated will provide important clues about the source of discovering new features for optoelectronic devices. Generally, there is a big asymmetry of electric field in Schottky barrier at M/S interface with the pn junction in semiconductor devices, and the differences of the amplitude and frequency characteristics will exist inevitably. This will provide the possibility to extract the information from the

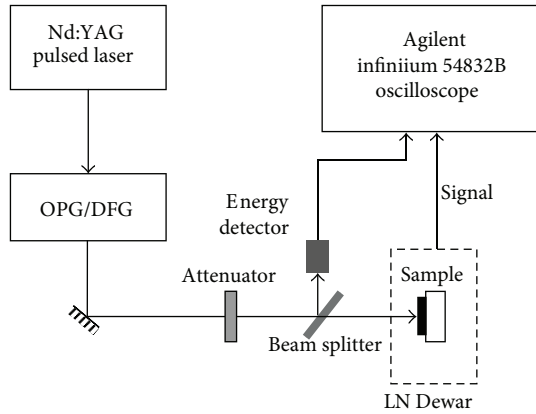


FIGURE 1: Schematic diagram of the transient photovoltage technology (not to the scale).

TPV. In this reason, this paper will carry out the detailed studies the of PV response of HgCdTe PV array utilizing TPV. The experiment results show an apparent negative valley first, then it evolves into a positive peak. By employing a combined theoretical model of pn junction and Schottky potential, this photo-response polarity changing curves can be interpreted well. Due to the Schottky barrier of M/S interface, the negative PV response induced will decrease the positive signal generated by pn junction, and consequently reducing the response rate. Since the characteristics of $p-n$ junction and Schottky barrier will interfere each other in the conventional $I-V$ test, it is very difficult to assess the quality of the electrode. While the characteristic can be distinguished by exploiting the TPV, this method may have an advantage compared with the conventional electrode assessment methods, and the sensitivity is expected to be greatly improved.

2. Experiment

The HgCdTe planar pn junction PV detector was grown by MBE on GaAs substrate with a buffer layer of CdTe. The acceptor and donor concentration were 8×10^{15} and $1 \times 10^{17} \text{ cm}^{-3}$, respectively. The Cd composition was 0.298 (the cutoff wavelength is approaching $4.8 \mu\text{m}$). The junction area was $50 \times 50 \mu\text{m}^2$. The experimental system consisted of four major parts: liquid nitrogen (LN) Dewar, wavelength tunable ultrafast pulsed lasers, energy monitoring system, and digital Storage oscilloscope, which is shown in Figure 1 [10, 11]. The sample was mounted in LN Dewar for measurement, and the temperature was near 77 K [10]. The incident laser pulse was provided by a Picosecond Nd:YAG laser (EXSPLA PG401/DFG). The Laser delivered pulse of 30 ps in duration at a frequency 10 Hz. Comparing to the shortest rising time of tens of nanoseconds in the pulsed response profile of the HgCdTe photodiode, the 30 ps laser pulse can be approximated as a δ function in our experiment. A small portion of the laser beam was reflected by a beam splitter and measured using an energy detector in order to monitor the exciting energy. The pulsed photo-response of the HgCdTe detector was measured from the voltage drop across a 50Ω

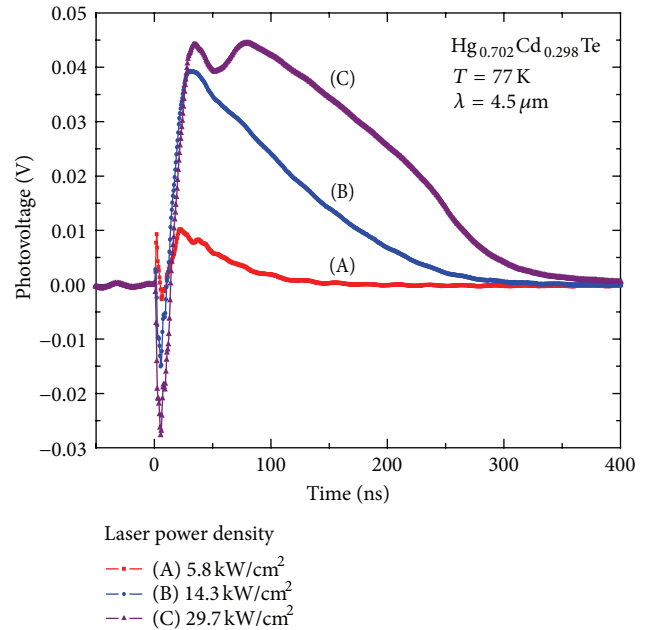


FIGURE 2: Transient PV response of the detector illuminated by the pulsed laser with the photon energy larger than the bandgap for the different incident intensity.

load-resistor. Both signals from the energy detector and the HgCdTe detector were fed into an oscilloscope through BNC connectors to monitor and record the pulse profiles. An average of 200 pulsed profiles was recorded to eliminate the pulse-to-pulse fluctuation and improve the signal to noise ratio. An aperture was used to limit the illumination area of the linear array detectors by blocking the laser beam.

3. Results and Discussion

The basic mechanism of n^+ -on- p HgCdTe PV photodiode is the following: The incident photon absorbed by p -HgCdTe layer will generate photo carriers. These carriers will be separated by the build-in electric field and form the photovoltaic response. Therefore, the ideal PV response should show a rapid increase and slow decay process [10]. However, the TPV response time profiles of the HgCdTe photodiode shows an apparent negative valley during the first 15 ns, and then it evolves a positive peak. By changing the excitation laser intensity, the transient photo-response of the detector shows the similar time evolution profiles, no matter for the case of one-photon absorption (OPA) transition that the photon energy is larger than the bandgap (shown in Figure 2) or for the case of two-photon absorption (TPA) transition that the photon energy is smaller than the bandgap (shown in Figure 3). This shows that there is a new mechanism for the photo-response polarity changing, where the phenomenon has been observed before [11]. For subsequent discussion and data analysis, some experimental results are listed here.

The negative TPV of experiment result can be attributed to the Schottky barrier at the metal-HgCdTe interface. Because the p - and n -electrodes of the array are in the same

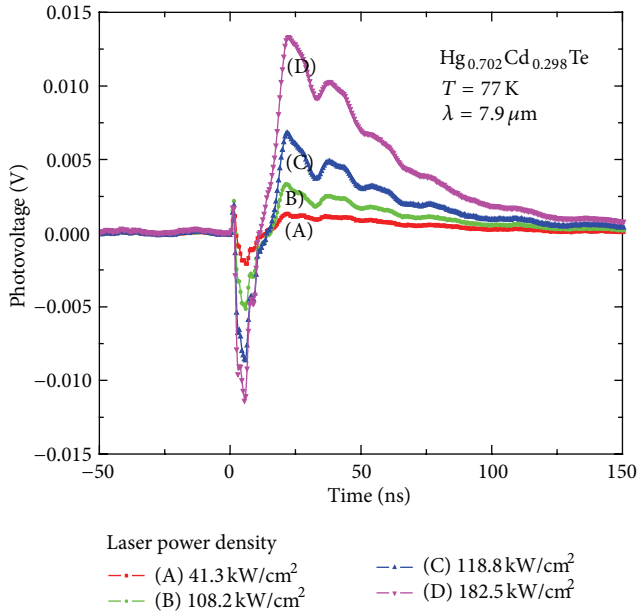


FIGURE 3: Transient PV response of the detector illuminated by the pulsed laser with the photon energy smaller than the bandgap for the different incident intensity.

plant, if a Schottky contact is formed at the interface of the metal layer with the *p*-HgCdTe surface, then it will constitute a class *n*⁺-on-*p* junction. The opposite built-in electric field of the Schottky barrier contact comparing to *pn* junction provides the possibility for the generation of negative valley and positive peak in the TPV, while the high-frequency characteristic of the Schottky barrier [12] provide the possibility for the generation of negative PV prior to positive ones.

The negative PV response derived from Schottky barrier mechanism of M/S interface can also be confirmed by the transient PV response experiment measurement with and without aperture added in the optical path for photon energy larger (OPA, shown in Figure 4(a)) and smaller (TPA, shown in Figure 4(b)) than the bandgap. For the array detector used in this experiment, the common *p*-electrode configurations surround all pixels in the linear array of the detectors. Because the size of pixel is only $2.5 \times 10^3 \mu\text{m}^2$, the spot of the incident laser reaches 50mm^2 , which is about 2×10^4 times larger than the pixel area. Thus the *p*-electrode covering area will be illuminated inevitably and even will constitute a major part of the light receiving area if the incident laser beam has been not limited by aperture. If a Schottky contact is formed at the interface of the metal layer with the *p*-HgCdTe surface, the magnitude of the negative TPV generated from M/S interface should be sufficient compare with that of *pn* junctions. However, the negative PV valley will be suppressed, and the positive PV will be enhanced when the size of the incident laser beam is limited by aperture. Thus, the ratio of negative valley to positive peak can be realized by limiting the illumination area of the array electrode. The experimental results demonstrate that the PV response effect of Schottky barrier at M/S interface is suppressed if the illumination area

of *p*-electrode interface is decreased. So the correctness of the combined theory model is verified.

From the discussion mentioned above, one can interpret this photo-response polarity changing TPV by employing a combined theoretical model of *pn* junction and Schottky potential. Since the Schottky barrier has the similar characteristic to *n*⁺-on-*p* junction and the TPV curves of *pn* junction show the form of a typical pulse function, the apparent TPV curves of the detector can be expressed as a superposition of two single pulse function:

$$V(t) = V_{\text{schottky}}(t) + V_{\text{pn}}(t) \\ = \Delta V_{\text{schottky}} \left[1 - \exp\left(-\frac{t}{\tau_1}\right) \right] \exp\left(-\frac{t}{\tau_2}\right) \\ + \Delta V_{\text{pn}} \left[1 - \exp\left(-\frac{t}{\tau_1'}\right) \right] \exp\left(-\frac{t}{\tau_2'}\right), \quad (1)$$

where $\Delta V_{\text{schottky}}$, τ_1 , and τ_2 are the photovoltage, pulse rise time, and fall time of Schottky contact, respectively. ΔV_{pn} , τ_1' and τ_2' are the photovoltage, pulse rise time and fall time of *pn* junction, respectively.

The dash line in Figure 5 is the best that fits with (1). The excellent fittings suggest a good reliability of the combined theory model of *pn* junction and Schottky barrier. The PV response curves of *pn* and Schottky barrier are also simulated respectively. The characteristic parameters values of transient photo-response are extracted from the fitting procedure. It can be seen that the response extremum, pulse rise time and fall time of the photovoltage generated by the Schottky contact are -68mV , 3.3ns and 20ns , respectively, while they are 82mV , 10ns and 80ns in *pn* junction. This shows that the pulse PV response generated by the Schottky barrier is negative and has a higher frequency characteristic respect to the *pn* junction ones. Thus the photo-response shows an apparent negative valley first, then it evolves into a positive peak. On the other hand, the negative PV response induced by the Schottky barrier will decrease the positive signal generated by *pn* junction, consequently reducing the response rate. As can be seen, although the simulation PV peak shown in Figure 5 is 55mV , the experimental PV peak is partially offset by the negative PV induced by Schottky contact to only 39mV , reducing the response rate to less than 70% of the simulation PV peak. If the performance of the electrode is poor, a larger Schottky barrier high between metal and the *p*-HgCdTe layers will exist at the interface. Thus, the negative PV will be more significant, even stronger than the positive PV. This is the reason why some HgCdTe photovoltaic devices appear to be anomalies negative open circuit voltage and the negative PV in the *I-V* test [13–15].

4. Conclusion

In summary, we have reported the effect of metal-semiconductor contact on the transient photovoltaic characteristic of HgCdTe PV detector. The Schottky barrier at the M/S interface cause the photo-response shows an apparent negative valley first, then it evolves into a positive

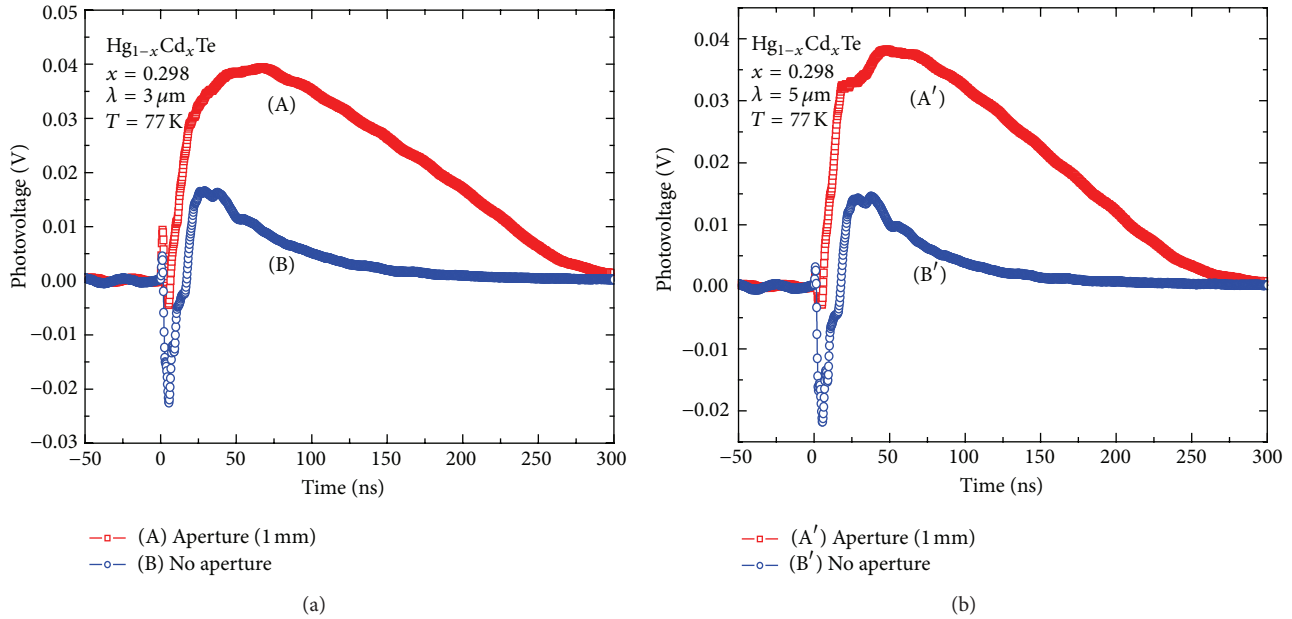


FIGURE 4: Transient PV response of the HgCdTe photodiode with no aperture and 1 mm aperture added in the optical path for incident photon energy larger and smaller than the bandgap.

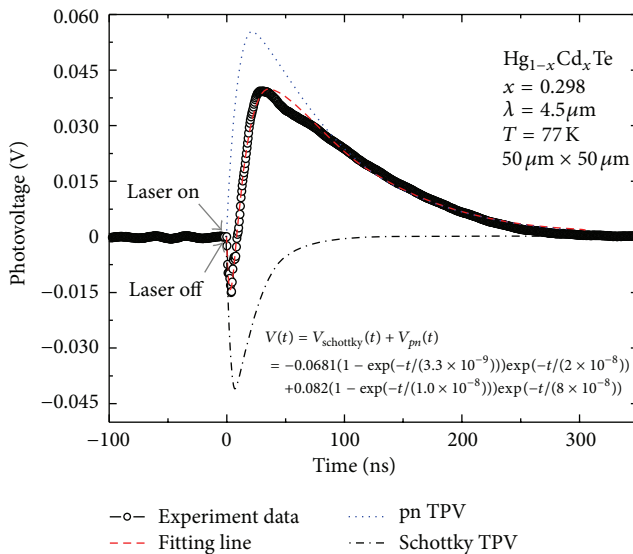


FIGURE 5: Pulsed PV response profiles from HgCdTe photodiode illuminated with $4.5\ \mu\text{m}$ laser pulses. The circle points are the experiment results, and the dash line is the fitting curve obtained by using the theory model. The dot line and dash dot line present the simulation of pn and Schottky potential PV response, respectively.

peak. By employing a combined theoretical model of pn junction and Schottky potential, the characteristic parameters of transient photo-response are extracted. Utilizing this TPV characteristic of device, we can evaluate the electrode quality at the interface of metal/HgCdTe. Compared with the conventional I - V test, it can distinguish the characteristic parameter from pn junction. Thus, our initial result on the effect of M/S would make such TPV test a potential candidate for electrode assessment methods.

Conflict of Interests

The authors declared that they have no conflict of interests to this work.

Acknowledgment

This work was supported by the National Natural Science Foundation of China (61107081, 61202369, and 61204105), Innovation Program of Shanghai Municipal Education Commission of China (12ZZ176).

References

- [1] W. D. Hu, X. S. Chen, Z. H. Ye et al., "Polarity inversion and coupling of laser beam induced current in As-doped long-wavelength HgCdTe infrared detector pixel arrays: experiment and simulation," *Applied Physics Letters*, vol. 101, no. 18, Article ID 181108, 5 pages, 2012.
- [2] W. D. Hu, X. S. Chen, Z. H. Ye, and W. Lu, "A hybrid surface passivation on HgCdTe long wave infrared detector with in-situ CdTe deposition and high-density hydrogen plasma modification," *Applied Physics Letters*, vol. 99, no. 9, Article ID 091101, 3 pages, 2011.
- [3] W. D. Hu, X. S. Chen, Z. H. Ye et al., "Dependence of ion-implant-induced LBIC novel characteristic on excitation intensity for long-wavelength HgCdTe-based photovoltaic infrared detector pixel arrays," *IEEE Journal of Selected Topics in Quantum Electronics*, vol. 19, no. 5, Article ID 4100107, 2013.
- [4] D. Y. Tang and Z. Y. Mi, *Introduction of Optoelectronic Devices*, Shanghai Science and Technology Literature Publishing House, Shanghai, China, 1st edition, 1989.
- [5] W. E. Spicer, D. J. Friedman, and G. P. Carey, "The electrical properties of metallic contacts on $\text{Hg}_{1-x}\text{Cd}_x\text{Te}$," *Journal of*

- Vacuum Science & Technology A*, vol. 6, no. 4, pp. 2746–2751, 1988.
- [6] W. E. Spicer, “Metal contacts on $\text{Hg}_{1-x}\text{Cd}_x\text{Te}$,” *Journal of Vacuum Science & Technology A*, vol. 8, no. 2, pp. 1174–1177, 1990.
- [7] X. N. Hu, Y. J. Li, and J. X. Fang, “Influence of MS interface transport on the current-voltage characteristic of MCV PV device,” *Journal of Infrared and Millimeter Waves*, vol. 20, no. 3, pp. 165–168, 2001.
- [8] X.-N. Hu, Y.-J. Li, and J.-X. Fang, “MS interface parameters extracted from current-voltage characteristic of PV device,” *Chinese Journal of Semiconductors*, vol. 22, no. 11, pp. 1439–1443, 2001.
- [9] V. Mikhelashvili, G. Eisenstein, V. Garber et al., “On the extraction of linear and nonlinear physical parameters in nonideal diodes,” *Journal of Applied Physics*, vol. 85, no. 9, pp. 6873–6883, 1999.
- [10] H. Y. Cui, Z. F. Li, Z. L. Liu et al., “Modulation of the two-photon absorption by electric fields in HgCdTe photodiode,” *Applied Physics Letters*, vol. 92, no. 2, Article ID 021128, 2008.
- [11] H.-Y. Cui, Z.-F. Li, F.-J. Ma, X.-N. Hu, Z.-H. Ye, and W. Lu, “Negative photovoltaic-responses in HgCdTe infrared photovoltaic detectors irradiated with picosecond pulsed laser,” *Journal of Infrared and Millimeter Waves*, vol. 28, no. 3, pp. 161–164, 2009.
- [12] J. Zhou, Y. Gu, Y. Hu et al., “Gigantic enhancement in response and reset time of ZnO UV nanosensor by utilizing Schottky contact and surface functionalization,” *Applied Physics Letters*, vol. 94, no. 19, Article ID 191103, 3 pages, 2009.
- [13] G. L. Zeng, S. Y. Chen, and D. He, “The I-V characteristic measurement, analysis and discussion of 8–14 μm HgCdTe PV detector,” *Infrared Technology*, no. 2, pp. 63–74, 1980.
- [14] G. H. Zeng, J. Sun, and L. Yan, “Analysis of current-voltage characteristics of the HgCdTe diodes with a parasitic pn junction,” *Infrared Technology*, vol. 18, no. 6, pp. 1–3, 1996.
- [15] S. X. Xing, Y. Cai, and B. K. Chang, “The analysis of HgCdTe loophole p-n junction’s abnormal characteristics,” *Infrared Technology*, vol. 24, no. 6, pp. 81–85, 2002.